Invited research article

LA-ICP-MS imaging in the geosciences and its applications to geochronology

David Chew[a,*], Kerstin Drost[a], Jeffrey H. Marsh[c], Joseph A. Petrus[b]

[a] Department of Geology, School of Natural Sciences, Trinity College Dublin, Ireland
[b] Harquail School of Earth Sciences, Laurentian University, Sudbury, ON, Canada
[c] Mineral Exploration Research Centre, Harquail School of Earth Sciences, Laurentian University, Sudbury, ON, Canada

A B S T R A C T

Laser ablation inductively coupled plasma mass spectrometry (LA-ICP-MS) mapping is a rapidly expanding field in the geosciences because of the wealth of spatial information it provides on the petrogenesis of igneous, metamorphic and sedimentary rocks and ore mineral formation. The technique has also opened many new applications in forensics, archaeology and the imaging of trace metals in biological tissues. Instrumentation advances in both LA and ICP-MS systems now permit precise isotopic analysis with laser spot sizes of < 10 μm and sub-ppm detections limits. In particular LA-quadrupole (Q)-ICP-MS systems facilitate mapping of large numbers of elements across nearly the entire mass range of the periodic table. A range of key applications in petrogenesis studies and in the fields of environmental and biological sciences is reviewed. Furthermore, technical considerations including a practical guide for setting up LA-ICP-MS multi-element mapping experiments and the latest innovations in dedicated data reduction and image processing packages for the visualization, interrogation and extraction of quantitative data from LA-ICP-MS maps are discussed, with particular emphasis placed on quadrupole systems. A key issue is imaging artefacts (spectral skew) caused by interaction between the laser repetition rate and the total sweep cycle time, particularly when coupling a sequential Q-ICP-MS analyser to modern low dispersion (fast-washout) LA cells. Running at high repetition rates is recommended for low-dispersion cells as it enables faster scanning while minimizing temporal variations in signal intensity caused by pulsing of the laser. Advances in LA-ICP-MS instrumentation and methodologies (data processing, visualization and extraction) have enabled simultaneous acquisition of compositional and U-Pb age information at high-spatial resolution which has great potential in geochronological studies. Formation histories of complex polyphase accessory minerals such as zircon, titanite or monazite, where discrete age domains are often linked with specific rock-forming processes and their physical conditions (i.e. U-Pb petrochronology), are now directly accessible. Moreover, fine-scale processes affecting the U-Pb systematics of accessory minerals can be constrained when LA-ICP-MS mapping is combined with other textural (e.g. CL or Raman) imaging techniques. U-Pb analysis of materials with variable initial Pb concentrations and/or heterogeneous genetic origin such as carbonates also benefit from such a mapping approach as areas with sufficient spread in ^{238}U/^{204}Pb ratio (μ) can be targeted, while simultaneous imaging of diagnostic trace elements allows identification and exclusion of zones affected by alteration or detrital contamination. The quasi-simultaneous detection offered by LA-time-of-flight (TOF)-ICP-MS allows rapid multi-element analysis of very fast transient signals (i.e. laser ablation imaging in low dispersion laser ablation cells). The approach is ideally suited to 2D and 3D imaging of biological and geological materials and will likely replace LA-Q-ICP-MS for such applications once more routinely available.

1. Introduction

1.1. LA-ICP-MS and other microbeam imaging techniques in the geosciences

LA-ICP-MS (laser ablation – inductively coupled plasma mass spectrometry) is an analytical technique that was developed over three decades ago for the *in-situ* determination of the elemental and isotopic compositions of geological and other solid materials (Sylvester and Jackson, 2016). Instrumentation advances in both LA and ICP-MS systems now permit precise analysis of elements at the ppm level with laser spot sizes of < 10 μm. A notable innovation in the last decade is the advent of 2D or 3D elemental or isotopic mapping by LA-ICP-MS (Woodhead et al., 2016). LA-ICP-MS image mapping is a rapidly expanding field in the geosciences because of the wealth of fine-scale
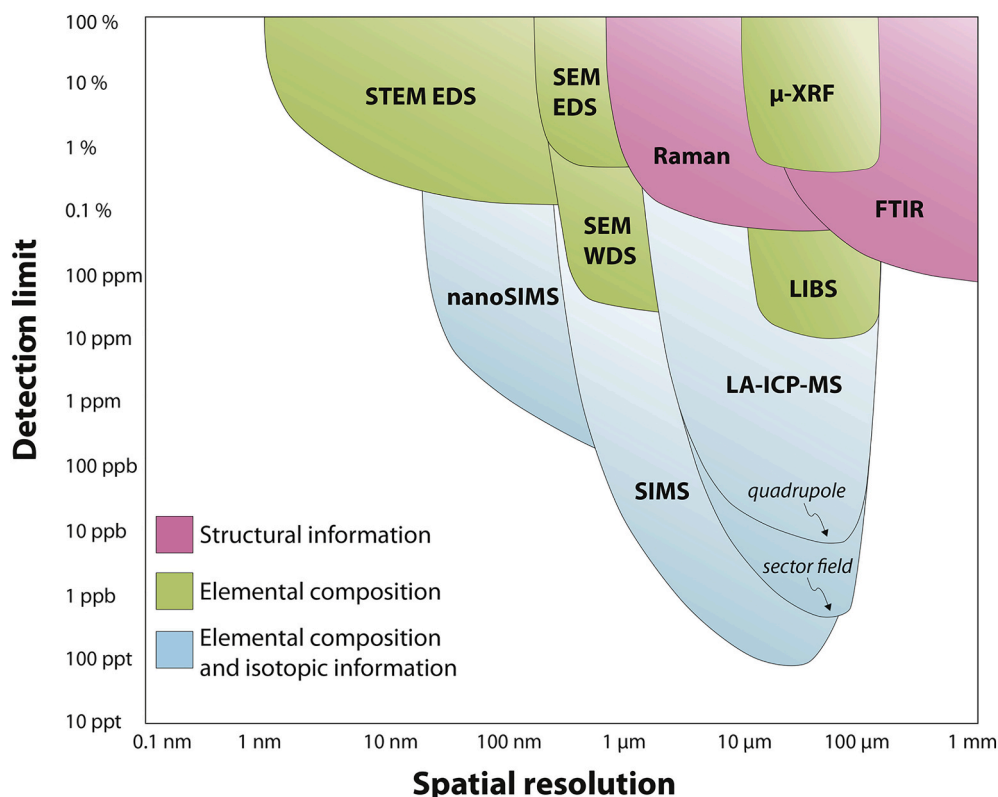
Fig. 1. Detection limit *vs* spatial resolution (x-axis) for the suite of microbeam methods commonly utilised by geoscientists, adapted from Li and Li (2016).

spatial information it provides on processes such as the petrogenesis of magmatic, metamorphic and sedimentary rocks and ore mineral formation. Additionally, given the critical role trace metals play in a variety of systems, the technique has also opened many new applications in different fields ranging from bioimaging of tissues to the material sciences. A comparison of LA-ICP-MS imaging versus other microbeam mapping techniques commonly employed by geoscientists is discussed below, while a suite of LA-ICP-MS imaging case studies are provided in section 2 and illustrate a highly diverse range of applications across the geological, environmental and biological sciences.

Advances in microbeam instrumentation have allowed the observation and measurement of the chemical and structural composition of solid materials with both increasing spatial resolution and improved detection limits. Fig. 1 illustrates detection limit (y-axis) *vs* spatial resolution (x-axis) for the suite of microbeam imaging methods commonly utilised by geoscientists. Various other approaches that are less routinely available such as synchrotron μPIXE and nano-XRF (particle induced X-ray emission and x-ray fluorescence) are not illustrated. Such synchrotron-based techniques typically provide ppm-level detection limits with sub-micron scale spatial resolution (e.g. Majumda et al., 2012), with the latest generation synchrotron nano-XRF instruments providing ppm-level sensitivity coupled with a spatial resolution down to 10 nm (Cesar da Silva et al., 2017). The most common microbeam methods utilized by geoscientists for mapping applications (SEM-WDS and -EDS, Raman, FTIR, SIMS, LA-ICP-MS) are described in detail in the sections below. Two other imaging techniques employed in geoanalytical laboratories are mentioned briefly here and are illustrated on Fig. 1. Laboratory μ-XRF facilitates mapping of large (hundreds of cm^2) samples with c. 10 μm resolution, although most commercially available systems are only capable of mapping major elements at reasonable sample throughputs. Laser-induced breakdown spectroscopy (LIBS) is also employed for elemental mapping of minerals down to the tens of ppm level (Fabre et al., 2018). It can be utilized either as a standalone instrument or in tandem with LA-ICP-MS, where it enables analysis of

elements such as C, H, O, N and F that are either challenging or impossible to analyse by LA-ICP-MS.

The choice of microbeam method is application dependent, and usually governed by the concentration of the target analyte(s) in the sample (e.g. whether the detection limit of the analytical method in question is at the major, minor or trace element level) and the analytical spot size. Further considerations include whether other information is required, such as chemical bonding, crystallographic or isotopic data and instrument availability, particularly in the case of synchrotron-based techniques.

1.1.1. SEM WDS and EDS

Quantitative determination of elemental compositions by x-ray microanalysis can be performed either on scanning electron microscopes (SEM) or electron microprobes (EPMA). Many SEM and EPMA instruments have energy dispersive spectrometers (EDS) mounted to the column, and an EPMA typically has an array of several wavelength dispersive spectrometers (WDS) for simultaneous measurement of multiple elements. They are both essentially non-destructive techniques permitting elemental analysis with micron-scale spatial resolution on standalone SEM instruments (Fig. 1) but differ in the means by which they separate X-rays; EDS sort the X-rays based on their energy, while WDS sort the X-rays based on their wavelengths. A WDS detector system has detection limits at the 10s of ppm level (Fig. 1) and spectral resolution which is an order of magnitude superior to that of EDS, and as such is often regarded as the "gold standard" of elemental microanalysis (Newbury and Ritchie, 2013). In addition, the higher probe current employed in WDS systems (typically 15-20 nA) generates significantly more X-rays (and hence counts) compared to EDS (the probe current in an EDS system is typically 100s of pA). However, the high probe current employed in WDS systems can induce significant time-dependent loss of volatile elements such as the alkalis and halogens (Morgan and London, 1996), while the number of elements that can be simultaneously acquired is physically limited by the number of WD

spectrometers mounted to the EPMA beam column.

EDS permits simultaneous quantification of all elements in the periodic table bar H, He, and Li. However, EDS systems on standalone SEM instruments suffer from high continuous bremsstrahlung background interference that decreases the signal to background ratio. EDS detection limits vary depending on the target element and analytical conditions, and a detection limit for many elements is typically quoted at the 0.1 wt% range (e.g. Kuisma-Kursula, 2000) although is often lower (c. 0.05 wt%) for elements such as Fe on the Kα line. Advanced pulse processor electronics that can account for photon coincidence on the detector at high count rates combined with multiple large format (> 150 mm^2) silicon drift detectors (SDD) mean that the latest generation multi-detector EDS systems are capable of element mapping at count rates up to 10 M counts per second (cps) and quantitative composition determinations at count rates approaching 1 Mcps. These modern SDD-based systems with their improved energy resolution and much higher count-rate ability can substantially increase the signal to background ratio and permit severe peak interference on both major and trace constituents to be accounted for by background removal using digital filtering (Ritchie et al., 2012). When SEM-EDS is performed under both standardised and controlled measurement conditions, measurement of trace constituents with limits of detection below 1000 ppm is now possible (Newbury and Ritchie, 2015).

1.1.2. Vibrational spectroscopic techniques (Raman and FTIR)

Raman and Fourier transform infrared absorption (FTIR) spectroscopy are both non-destructive, vibrational spectroscopic techniques. Raman spectroscopy is based on the inelastic scattering of light (Raman scattering) that allows for micron-scale characterisation of minerals and other materials. It can be measured across the spectral range, although it is most commonly measured in the ultraviolet, visible or near infrared regions. Raman spectroscopy has primarily been used in the geosciences for routine identification of minerals and the characterization of solid, fluid and gas inclusions. While it does not yield elemental composition information, it offers the advantage compared to SEM-EDS or WDS in that it is able to distinguish between chemically identical polymorphs or mineral phases with very similar chemistry. Raman spectroscopy has also been utilized in diverse applications such as characterization of radiation damage (metamictization) in zircon (e.g. Nasdala et al., 2002) or for thermometry estimates in (meta)sedimentary rocks by determining the progressive graphitization of carbonaceous material with increasing temperature (Beyssac et al., 2002). Recent developments include fast hyperspectral imaging of complex samples where a full Raman spectrum is collected at every pixel. When applied to natural zircon crystals such images mainly show the distribution of radiation damage (Nasdala et al., 2002; Chew et al., 2017), while rapid acquisition of Raman spectra is also now enabling automated phase mapping of minerals (e.g. Lünsdorf et al., 2019). Micro-FTIR compares the returned or transmitted light energy of the infrared (IR) spectrum to that of the emitted source spectrum, thus producing a spectrum of the IR energy absorbed by the sample (a solid, liquid or gas). It can provide information on the molecular structure of organic and inorganic components, and has been applied to the characterization of macerals and degree of thermal maturation in coal, characterization of individual organic material components in shale including kerogen, and the determination of volatile contents (primarily H_2O and CO_2) in minerals and glasses (e.g. Chen et al., 2015). The spatial resolution of μFTIR is typically on the order of 10s of μm due to the relatively large aperture size using a conventional light source but can be reduced down to 3–5 μm using a synchrotron radiation source (Della Ventura et al., 2010). The advent of focal plane array (FPA) detectors with multi-channel detection has facilitated rapid μFTIR imaging with a spatial resolution as low as 5 μm (Chen et al., 2015). Both Raman and FTIR can now achieve nano-scale resolution through approaches such as tip-enhanced Raman scattering (TERS) microscopy and IR scattering scanning near-field optical microscopy (s-SNOM).

1.1.3. SIMS and comparison with LA-ICP-MS

Secondary-ion mass spectrometry (SIMS) and LA-ICP-MS are the two main microbeam techniques utilized by geoscientists for the analysis of trace elements and isotopic compositions in solid materials. SIMS and its capabilities relative to LA-ICP-MS are primarily discussed here, as the principles behind LA-ICP-MS are covered in more detail in section 1.2. SIMS instruments sputter the surface of a specimen with positive (e.g. Cs) or negative (e.g. O) ions and then collect and analyse the ejected secondary ions. The majority of SIMS instruments employed in geoscience applications typically utilize dynamic (high primary current density), large-geometry sector-field mass spectrometers with multi-collector detection. Such instruments when equipped with multiple Faraday detectors are capable of analytical uncertainties of approximately 0.1% on isotopic ratios and detection limits which vary according to the target element, matrix and analytical conditions, but are typically significantly below 100 ppb for elements such as Pb (Stern, 2009). SIMS is often regarded as the gold standard for *in-situ* U-Pb geochronology, and a particular advantage is the small analytical pit volume, which is typically 10–20 μm wide and 1.5–2 μm deep for U-Pb zircon analyses (e.g. Kröner et al., 2014). In contrast, while the analytical pit diameter is typically only slightly broader (c. 25 μm) in LA-ICP-MS multi-collector (e.g. Hopkinson et al., 2017) and quadrupole (Arboit et al., 2019) U-Pb zircon dating studies, the pit depth is substantially greater, typically c. 15 μm.

Large-geometry SIMS instruments are capable of micron-scale element distribution mapping, and the full U-Pb isotopic systematics of zircons (Hadean zircons from the Jack Hills metasedimentary belt) have been imaged on a < 5 μm scale by SIMS scanning ion imaging (Bellucci et al., 2018). The theoretical limits to the lateral spatial resolution during sputtering is on the order of 10 nm (Stern, 2009), but similar to LA-ICP-MS, low analyte volumes come at the expense of significantly increased analytical uncertainty. Nano-SIMS instruments were developed to produce an ion beam with a significantly reduced spot size (c. 50 nm for Cs$^+$ and 150 nm for O$^-$ ions respectively) compared to large-geometry SIMS, while retaining high levels of analytical sensitivity. Applications that have utilized the high sensitivity and lateral resolution of NanoSIMS include imaging the isotopic fractionation of pre-Solar grains in meteorites, mapping characteristic biological signals (both chemical and isotopic) in geological samples at a sub-micron scale, and diffusion modelling of minor and trace elements in magmatic phenocrysts (Kilburn and Wacey, 2015). NanoSIMS ion imaging with a spatial resolution of 50–100 nm has also been used to image Pb nanospheres in Archean zircons which formed due to Pb mobilization during metamorphism, with the technique capable of resolving the timing of nanosphere formation from the age of host zircon crystallization (Lyon et al., 2019).

1.2. Principles of LA-ICP-MS and the development of LA-ICP-MS imaging

Laser ablation is the process whereby laser radiation interacts with an attenuating solid, breaking down chemical bonds and resulting in removal of material from the sample surface, ideally while minimizing melting and other thermal reactions at the ablation site. The resultant vapour plume of ablation products (an aerosol) is swept out of the ablation cell into the ICP-MS instrument using a carrier gas (normally He or Ar). The volume of material removed by a single laser pulse depends on various parameters such as the optical (e.g. absorbance and reflectivity) or thermal (e.g. heat capacity and conductivity) properties of the material (Günther and Hattendorf, 2005), the laser fluence, wavelength and pulse length. In the geosciences, pulsed (nano- or femtosecond), short wavelength (typically deep UV) lasers are typically employed; both shorter wavelengths (Jochum et al., 2007) and pulse lengths (Jochum et al., 2014) have been shown to reduce elemental fractionation between different matrices. The ablation cell is typically housed on a sample stage that can move in the X, Y and Z directions while the laser beam is stationary. Modern LA systems have typical

Table 1
Laser parameters employed in the applications listed in Section 2

Authors	Beam size	Scan speed	Repetition rate	Analysed material
Astbury et al., 2018	10-30 μm	4 - 12 μm/s	8 Hz	feldspar and pyroxene
Austin et al., 2013	30 μm	30 μm/s	20 Hz	primate teeth
Bonnetti et al., 2020	5 μm	10 μm/s	40 Hz	pyrite from a roll-front uranium deposit
Bussweiler et al., 2015	20 μm	5 μm/s	10 Hz	olivine
Dare et al., 2014	15-19 μm	4 μm/s	10 Hz	magnetite
Draxler et al., 2015	50 μm	20 μm/s	10 Hz	rat bone
Evans and Müller, 2013	20-25 μm	16.6 - 25 μm/s	10 - 15 Hz	benthic foraminifera
Gallagher et al., 2015	80 μm	50 μm/s	4 Hz	pyrite
Genna and Gaboury, 2015	15 μm	5 or 10 μm/s	10 Hz	pyrite
George et al., 2018	17 μm	5 μm/s	10 Hz	garnet
Hare et al., 2017	30 μm	120 μm/s	n/a	mouse brain tissue
Henrichs et al., 2018	7 μm	6 μm/s	100 Hz	apatite, metabasite matrix
Henrichs et al., 2019	7 μm	6 μm/s	100 Hz	apatite, epidote/allanite
Hnatyshin et al., 2020	100 or 20 μm	100 or 20 μm/s	10 Hz	pyrite in rock fragment
Jankovics et al., 2019	5-15 μm	0.5 × spot size / s	8 Hz	olivine
Kaeter et al., 2018	7, 10 or 18 μm	10 μm/s (7 or 10 μm spots) or 30 μm/s (18 μm spots)	55 Hz	muscovite, albite and columbite group phases
Large et al., 2009	15 or 25 μm	15 or 25 μm/s	10 Hz	pyrite
Li et al., 2020	6 μm	6 μm/s	100 Hz	Fe-Mn micronodules
Moreno-Gordaliza et al., 2011	8-100 μm	10-150 μm / S	20 Hz	rat kidney tissue
Petrus et al., 2017	7-30 μm	6-150 μm/s	8-50 Hz	Mn crust, peridotite, clinopyroxene, zircon
Raimondo et al., 2017	16 μm	22 μm/s	10 Hz	garnet
Stead et al., 2017	30 μm	n/a	60 Hz	olivine and clinopyroxene
Ubide et al., 2015	12 or 24 μm	between 0.5 - 1/5 μm spot size / s	2-12 Hz	clinopyroxene and amphibole
Ubide and Kamber, 2018	12, 20 or 24 μm	1.5 × spot size / s	10 Hz	clinopyroxene
Ubide et al., 2019a	10 or 20 μm	10 or 20 μm/s	10 Hz	clinopyroxene
Ulrich et al., 2009	30 - 80 μm	typically 0.5 × spot size / s	10 Hz	garnet, meteorite impact breccia, sulphides, oolith
Van Malderen et al., 2017b	20 μm	200 μm/s	150 Hz	wheat and rye grains
Woodhead et al., 2007	157 μm, 71 μm	300 μm / s (157 μm spot), 9.5 μm / s (71 μm spot)	5 Hz	stalagmite, otolith
Yao et al., 2019	5 or 10 μm	0.5 × spot size / s	5 Hz	chromite with sulphide inclusions
Zhou et al., 2017	2-35 μm	20-200 μm/s	10-40 Hz	pyrite
Zhu et al., 2016	60 μm	50 μm/s	n/a	pyrite vein in matrix

stage reproducibility better than 1 μm, and spot sizes ranging from as large as 200 μm down to 1 μm.

The plasma source of an ICP instrument is sustained by a radio frequency (RF) generator which can ionize the vast majority of the elements of the periodic table when using Ar as a plasma gas; exceptions include H and unless negative ion mode is available, elements with a higher first ionization potential than Ar (e.g. He, Fe and Ne). Ions produced in the ICP pass through a low-vacuum sampling interface consisting of two metallic cones (the sampling cone and the skimmer cone), to the mass analyser (typically a quadrupole or magnetic sector). Quadrupole mass analysers are sequential, while magnetic sector field instruments can be fitted with a single sequential collector for elemental/isotope ratio analysis or multiple collectors (MC-ICP-MS) to facilitate simultaneous detection of ion beams for high-precision (as low as 0.02%; Gu et al., 2019) isotope ratio analysis. The potential of ICP time-of-flight (TOF) mass analysers and double-focusing sector field ICP-MS based on a Mattauch-Herzog geometry for simultaneous measurement of all elements is discussed further in section 5.

LA-ICP-MS analyses have conventionally used static single spot ablations ever since the first ICP-MS studies that employed laser ablation for sample introduction (Gray, 1985). LA-ICP-MS maps can be constructed as a grid of spots and therefore theoretically LA-ICP-MS imaging has been possible for several decades, but such an approach is extremely time consuming (cf Kelly et al., 2017) and hence is rarely undertaken. Instead, LA-ICP-MS imaging is typically carried out by rastering the laser beam across the sample surface (e.g. continuous movement of the stage under the fixed ablation site), and the full elemental or isotopic map is constructed from the time-resolved signals derived from successively ablating adjacent lines (e.g. Ubide et al., 2015). Time-resolved elemental concentration profiles utilizing laser ablation line scans ("rasters") have been employed in geological applications since the late 1990s (Košler, 2008), and the first geological LA-ICP-MS imaging applications constructed from tightly-spaced line scans followed shortly after (e.g. Treble et al., 2005).

However, significant uptake of the method was only made possible by several key developments in instrumentation and data reduction approaches (Woodhead et al., 2016). These include the advent of (i) low dispersion (fast washout), two-volume cells (e.g. Eggins and Shelley, 2002) and transport-tubing assemblies for rapid introduction of the sample aerosol into the ICP (e.g. Van Malderen et al., 2016) which both minimize smearing of the signal as the laser beam is rastered over elemental concentration gradients; (ii) the advent of high repetition rate lasers, which confer many advantages in LA-ICP-MS mapping (e.g. section 3.2), (iii) improved functionality of the software that controls laser ablation systems including the ability to export laser log files containing timestamps and stage positions when the laser is turned on and off; and (iv) improved LA-ICP-MS data reduction packages which can produce elemental or isotopic ratio maps and which can include the ability to import time-stamped laser logfiles along with a wide variety of ICP-MS data formats. A range of both in-house and commercial software packages available for the reduction of LA-ICP-MS image data and the production of LA-ICP-MS elemental or isotopic ratio maps are summarized in Weiskirchen et al. (2019). Such packages include Iolite (Hellstrom et al., 2008; Paton et al., 2011), SILLS (Guillong et al., 2008), LAICPMS (Rittner and Müller, 2012), AERYN (Mouchi et al., 2016), LA-iMageS (López-Fernández et al., 2016), TERMITE (Mischel et al., 2017), iQuant2 (Suzuki et al., 2018), HDIP (Teledyne CETAC Technologies, 2020) and LA-ICP-MS Image Tool (Managh and Reid, 2019). A series of geological, environmental and biological LA-ICP-MS imaging application are provided in section 2 below while detailed technical considerations for the production of LA-ICP-MS maps are discussed in section 3.

2. Example applications

The applications of LA-ICP-MS image mapping in the geosciences are highly diverse (Woodhead et al., 2016), extending from the petrogenesis of magmatic, metamorphic and sedimentary rocks and ore
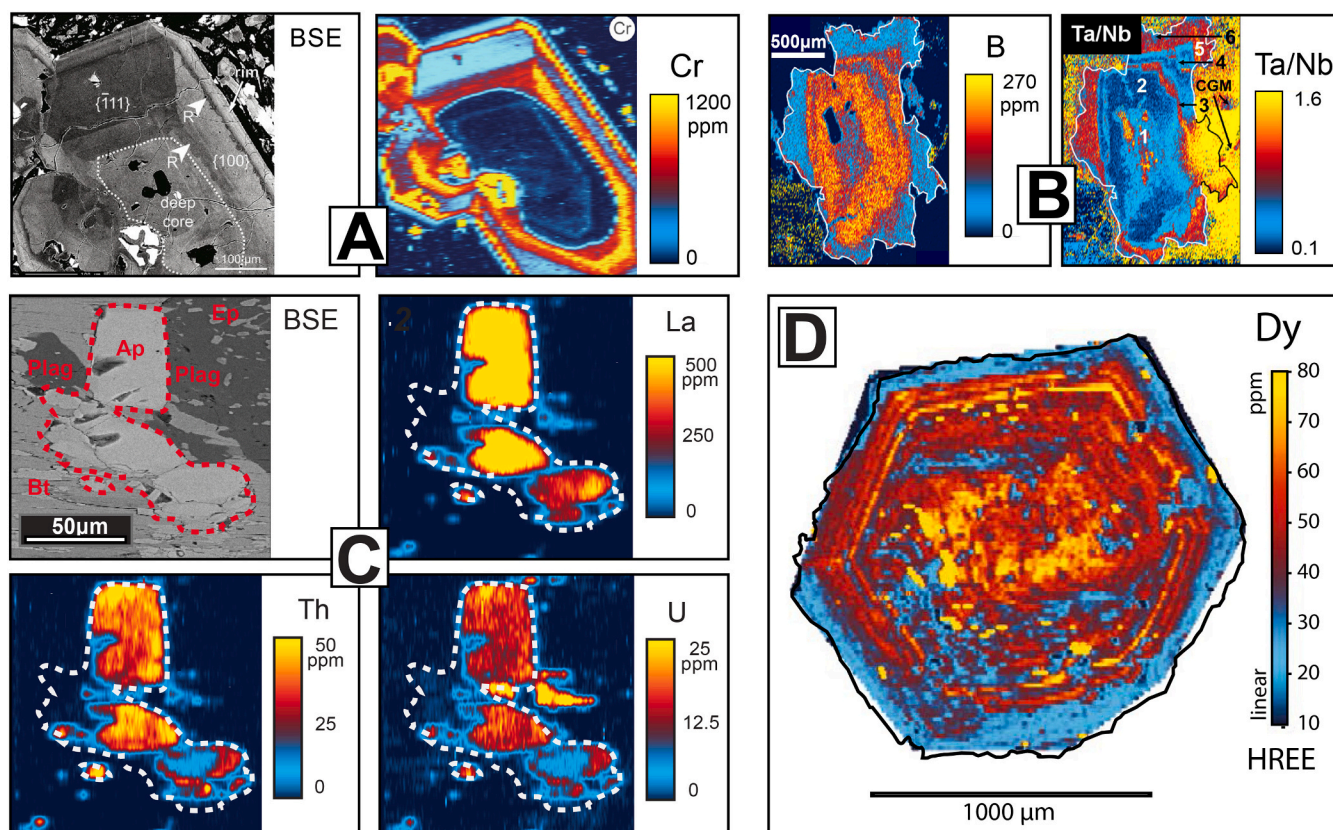
Fig. 2. LA-ICP-MS trace-element imaging of igneous and metamorphic phases. A) BSE and LA-ICP-MS map of titanaugite from trachybasalt at Mount Etna (modified from Ubide et al., 2019a). The crystal has an anhedral core that shows an irregular contact with the sector-zoned mantle. 'R' (in BSE image) indicates Cr-rich zones that represent recharge by a more mafic magma. B) LA-ICP-MS map of minor and trace elements (B, Tb/Na) in muscovite from the Leinster pegmatite belt (Ireland) at the contact between the Caledonian Leinster batholite and Ordovician host rocks (modified from Kaeter et al., 2018). Six growth zones identified from element maps are indicated on the Tb/Na map; CGM denotes columbite-group minerals. C) BSE and LA-ICP-MS maps of apatite from the Variscan Central Aar granite in the Swiss Alps from Henrichs et al. (2019). The apatite cores yield Variscan ages and a chemistry consistent with an I-type granite affinity, while the rims are depleted in REE and the actinides and have a low-grade metamorphic affinity (*cf* O'Sullivan et al., 2020) consistent with Alpine dissolution-reprecipitation under greenschist-facies conditions. D) HREE (Dy) map of a garnet-grade metapelite from the Sikkim Himalaya from George et al. (2018). The core shows limited Dy (and other HREE + Y) mobility and mimics the pre-existing matrix, while the outer oscillatory zoning shows an increase in the length-scale of equilibration of HREE + Y along the garnet–matrix interface.

mineral formation (sections 2.1 - 2.4) through to geochronology (section 4). The laser analytical conditions and the analysed matrices described in sections 2.1 - 2.4 are listed in Table 1. The technique has also opened many new applications in different fields ranging from environmental studies, bioimaging of cells (section 2.5) to the material sciences.

2.1. Magmatic systems

LA-ICP-MS trace-element mapping has been employed in combination with other methods (such as microscopy, SEM imaging, EPMA analysis, whole rock/mineral geochemistry, geothermobarometry) to shed light on a variety of processes in igneous systems. So far, LA-ICP-MS mapping has mostly been applied to reveal micron-scale trace-element zonation in macrocrysts from (sub-)volcanic rocks. Such studies on the growth stratigraphy of crystals have been carried out on amphibole, clinopyroxene (Fig. 2a), plagioclase, K-feldspar and olivine crystals to get insights into magma histories, eruption triggers, eruption time-scales, ascent rates and depth of magma storage (e.g., Ubide et al., 2015; Ubide and Kamber, 2018; Astbury et al., 2018; Ubide et al., 2019a; Jankovics et al., 2019). In addition, LA-ICP-MS trace element mapping has been applied to investigate rare earth element partitioning and sub-solidus exchange behaviour in olivine (Stead et al., 2017), while Bussweiler et al. (2015) used detailed petrographic and geochemical analyses including mapping experiments on olivine crystals

from kimberlites to distinguish multi-source olivine cores that formed in the mantle (xenocrysts) from multi-stage rims that formed in response to changing magma conditions (phenocrysts).

Furthermore, there can be considerable overlap between magmatic systems (this section) and ore systems (section 2.4.) Examples of studies at the interface between these systems include the work of (i) Dare et al. (2015) who used trace element concentrations and the results of mapping experiments on magnetite crystals of the El Laco magnetite deposits (Chile) to rule out a magmatic origin from effusive Fe oxide liquids for the deposit; (ii) Yao et al. (2017), who studied sulphide-silicate assemblages within chromite grains from the UG2 chromitite of the Bushveld igneous complex to argue for the coexistence of sulphide and silicate melts during chromite crystallisation with a model of magma mixing with felsic melt favoured to achieve chromite saturation, and (iii) Kaeter et al. (2018), who investigated the complex processes of crystal–melt–fluid interactions based on imaging and quantification of trace elements in muscovite- and columbite-group minerals during the magmatic-hydrothermal transition in rare element-bearing pegmatites (Fig. 2b).

2.2. Metamorphic systems

LA-ICP-MS trace-element mapping of metamorphic porphyroblasts is a promising application of the technique, as trace elements in metamorphic rocks are more sensitive than major elements to geochemical

interactions involving the entire mineral assemblage, including the growth and/or breakdown of accessory minerals, and are also typically less prone to diffusive resetting (Kohn, 2014; Raimondo et al., 2017). Ideally, trace-element mapping studies should investigate metamorphic phases stable over a range of P-T conditions and which preserve chemical information that can be related to the growth and breakdown of minerals associated with changing P-T and fluid conditions during metamorphism. The main mineral hosts for trace elements in metamorphic rocks include epidote-allanite (REE, Th, U, Sr), garnet (Y and the heavy REE [HREE]), phengite (Cs, Rb, Ba, B), titanite (Ti, Nb, Ta, REE), rutile (Ti, Nb, Ta), apatite (REE, Sr), monazite (Th, U and the light REE [LREE]) and zircon (Zr, Hf, Y, Th, U, Nb and Ta and the HREE).

Epidote is stable from the lower greenschist- to blueschist- and eclogite-facies conditions, and controls most of the REE and Th budget during HP-LT (El Korh et al., 2009) and Barrovian (intermediate P-T) metamorphism (Henrichs et al., 2018) of basic protoliths. Epidote, allanite (an epidote-group mineral rich in REEs, Sr, Th and U) and monazite dominate the REE budget in regional metamorphism of pelites, with allanite typically breaking down to form monazite (a LREE phosphate) in the amphibolite-facies (Corrie and Kohn, 2008). Phengite plays an important role in controlling the large ion lithophile element (LILE) budget during HP-LT metamorphism (El Korh et al., 2009). Of the Ti-bearing phases, rutile is stable at the highest pressures and lowest temperatures, titanite at intermediate P–T (Barrovian) conditions, and ilmenite at the lowest pressures and highest temperatures (Kohn, 2017). Rutile is an important carrier of the high field strength elements (HFSE) and controls Nb and Ta budgets in HP-LT metamorphism and subduction zone processes (e.g. Brenan et al., 1994), while titanite can contain significant REE, HFSE and Sr in Barrovian metamorphism of pelites, metaigneous and calc-silicate rocks. Apatite can also contain high REE and actinide abundances in high-grade and anatectic pelites (O'Sullivan et al., 2020), particularly when compared to apatite in low-grade pelites and meta-granitoids which is depleted in the REE and actinides due to coeval growth of epidote or monazite (Fig. 2c; Henrichs et al., 2018, 2019).

Garnet is a particularly attractive phase for LA-ICP-MS trace element mapping because (i) it frequently exhibits compositional zoning resulting from garnet-forming reactions linked to changes in P-T conditions, (ii) there is strong partitioning of many trace elements into garnet which are less prone to diffusional resetting then major elements, (iii) it has a large stability field in P-T space, and (iv) the growth and breakdown of accessory phases can be directly linked to garnet growth (Raimondo et al., 2017). The LA-ICP-MS garnet mapping experiments of Raimondo et al. (2017) from the Peaked Hill shear zone, central Australia show significant decoupling between major and trace-element zoning patterns, with smooth radial zoning in Fe, Mg, Ca and Mn and discrete oscillatory zoning of the REEs and Cr. The REE growth zoning and its subsequent subtle re-equilibration can be linked to a detailed sequence of growth and dissolution events and integrated with temporal constraints from geochronometers. George et al. (2018) investigated complex trace element growth zoning in garnet porphyroblasts from a garnet-grade metapelite from the Sikkim Himalaya. Garnet cores show limited HREE + Y equilibration due to a combination of HREE + Y immobility and their relatively slow diffusivities in garnet, resulting in compositional mimicry of the pre-existing matrix within garnet cores (Fig. 2d). Later oscillatory zoning requires an increase in the length-scale of equilibration of HREE + Y along the garnet–matrix interface (Fig. 2d), with the garnets thus showing a complex integrated record of the interplay between variable element equilibration, changing garnet growth rates and rock deformation which would be undetectable by major element analysis alone.

2.3. Sedimentary systems (clastic and carbonate)

The application of LA-ICP-MS elemental imaging to clastic and carbonate sedimentary systems is somewhat limited, despite the technique having great potential in yielding high-resolution spatial data for both trace element proxies of the water-column (such as biogenic and inorganically precipitated carbonates) and pore-water chemical and redox conditions (i.e. texturally later cements). LA-ICP-MS elemental imaging was applied by Ulrich et al. (2009) to examine trace element distributions in a late Archaean oolitic grainstone, and by Webb and Kamber (2011) to (i) abiogenic laminated carbonates from the early Neoproterozoic Little Dal Group, with the spatial chemical information supporting sedimentological arguments implying an abiogenic origin, and (ii) an Upper Devonian carbonate formed of the reef-constructing calcareous algae *Renalcis,* where the elemental maps identify the cryptic outline of calcified microbial communities from later generations of infilling cement. Gallagher et al. (2015) imaged the trace metal inventories of microbial carbonate-hosted pyrite from ca. 2.65–0.52 Ga, which demonstrated an increase in the shallow-marine Mo inventory across the pre-Cambrian–Cambrian boundary, and elevated Ni concentrations in the shallow marine Neoarchaean and early Palaeoproterozoic oceans which was attributed to a greater proportion of Mg-rich volcanic rock on land. The technique has yet to be applied in detail to cement growth histories but has promise in visualising trace element distributions in cements and facilitating correlation with cement stratigraphy parageneses derived from petrographic observations such as cathodoluminescence (CL) (*cf* Rusk et al., 2011).

2.4. Ore systems

Trace-element imaging by LA-Q-ICP-MS has become a widely used tool in studying ore systems, with applications ranging from prospecting tools (e.g. vectoring for mineral exploration), metallurgical applications such as ore beneficiation, to basic research questions such as ore petrogenesis and their timing. Due to its ubiquity and ability to incorporate a variety of trace elements, pyrite is ideally suited for ore exploration and petrogenesis studies utilizing LA-ICP-MS imaging. A key early application of the technique was by Large et al. (2009), who revealed gold and trace-element zonation in pyrite and demonstrated multiple stages of gold enrichment in the genesis of orogenic and Carlin-style sediment-hosted gold deposits. The approach has now been applied to numerous ore systems (e.g. Agangi et al., 2015; Cave et al., 2019; Conn et al., 2019; Cook et al., 2013; Gourcerol et al., 2018a; Steadman et al., 2015; Wu et al., 2018; Zhao et al., 2020; Bonnetti et al., 2020), often in combination with optical microscopy, SEM and EPMA analyses, Raman spectroscopy or other *in situ* microbeam techniques (e.g. S, Pb and Fe isotope measurements).

Recent applications include Genna and Gaboury (2015), who employed LA-ICP-MS trace-element imaging of pyrite to decipher the evolution of the mineralizing hydrothermal system in a replacement-type Archean volcanogenic massif sulfide deposit. Five pyrite types from specific ore zones of the deposit and from later metamorphic pyrite were distinguished, and discrimination diagrams employing As, Tl and Se data were proposed as an exploration tool for vectoring to the ore. Re/Os geochronology is an important tool for developing and confirming genetic models of ore systems; Hnatyshin et al. (2020) mapped and quantified Re distributions in pyrite in carbonate-hosted Zn-Pb ores to further understanding of the Re-Os systematics of pyrite-bearing ore. Pristine pyrite in the studied samples was shown to have Re concentrations of 1 to 10 ppb, while altered sulfides, fracture-fill material and secondary molybdenite all significantly increase the Re budget (Fig. 3a, b) thus hindering reliable Re-Os geochronology when such material is present in mineral separates. Additionally, the potential of S isotope mapping in pyrite by LA-MC-ICP-MS was explored by Zhu et al. (2016) and applied to a late-stage pyrite vein sitting in a matrix dominated by magnetite and siderite and containing interstitial early-stage pyrite and main ore-stage pyrite. The late-stage vein pyrite is clearly distinguished from the matrix on a $\delta^{34}S_{V-CDT}$ map and is similar to $\delta^{34}S_{V-CDT}$ spot analyses and to bulk analyses of the same material,
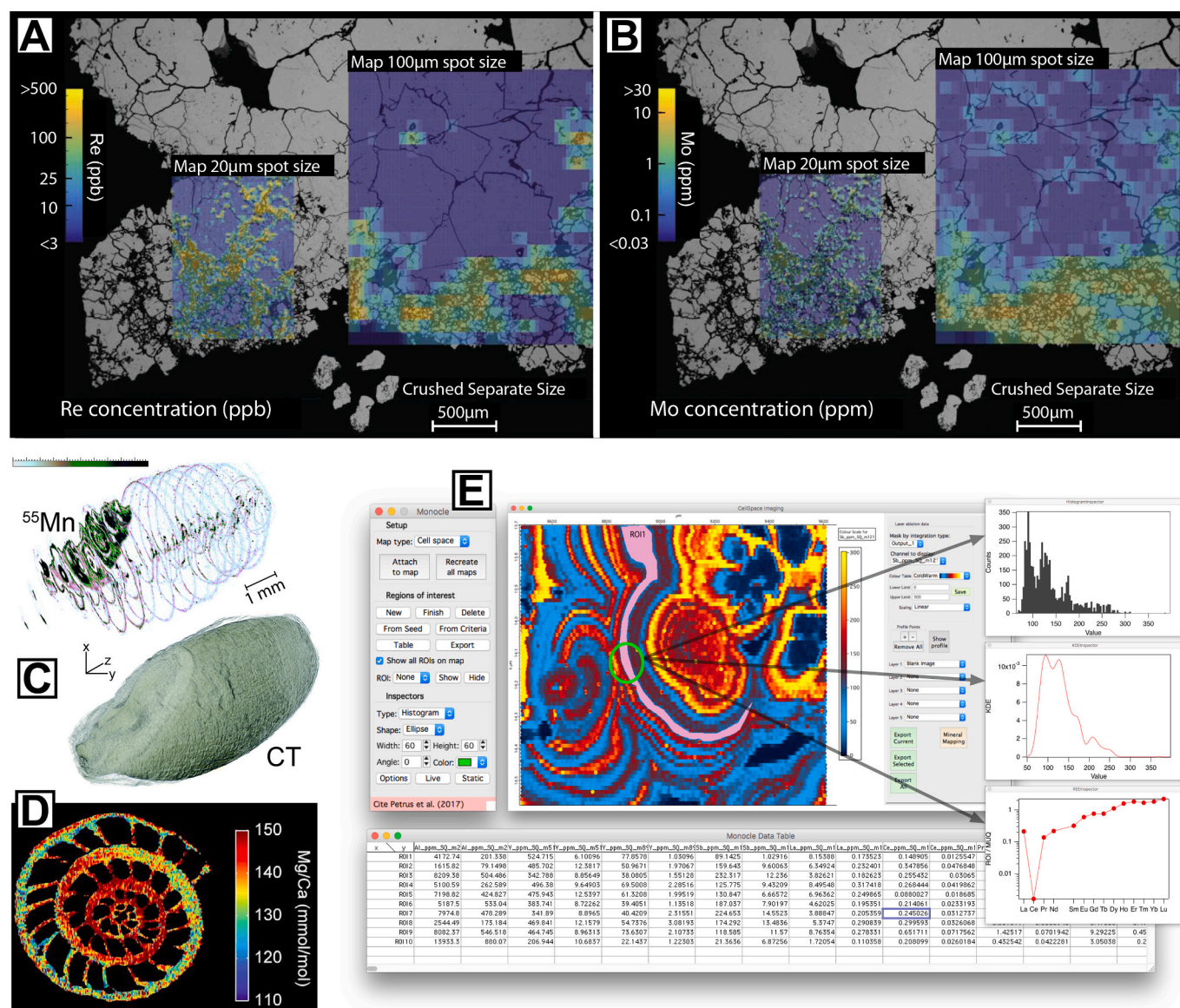
Fig. 3. LA-ICP-MS trace-element imaging of ore phases and biological / environmental samples. A) Rhenium and B) Mo concentration maps overlying a BSE image of a pyrite crystal from Hawker Creek (Mesoproterozoic Borden Basin, Baffin Island, Nunavut, Canada) showing a pristine low-Re core and fractured zones with elevated Re and Mo due to secondary processes (modified from Hnatyshin et al., 2020). C) 3D distribution of ^{55}Mn (a micronutrient) in mature wheat (*Triticum aestivum* L.) produced by LA-ICP-MS mapping and a serial sectioning approach, along with a micro-CT image of the wheat grain. Modified from Van Malderen et al. (2017a). D) LA-ICP-MS Mg/Ca map of a recent *Operculina ammonoides* showing seasonal Mg/Ca incorporation. The specimen mineralised from late summer to spring with a clear decrease from high Mg/Ca values (correlating with higher temperatures) in the earliest-formed central chambers towards the outside of the test. Modified from Evans and Müller (2013). E) Trace element systematics of a bulb-shaped Mn crust reflecting alternating periods of precipitation from variably intense hydrothermal input. The screenshots also highlight the basic functionality of Monocle (Petrus et al., 2017; Section 3.3), an interrogation tool for 2D LA-ICP-MS element and isotope maps which runs within the Iolite LA-ICP-MS data reduction software. The screenshots show the main Monocle window; real-time inspector tools with histogram, kernel density estimate and normalised REE patterns, and the Monocle data table export. Modified from Petrus et al. (2017).

demonstrating the feasibility of the technique.

LA-ICP-MS imaging has also been applied to a variety of ore and gangue minerals beyond pyrite. These include (but are likely not limited to) magnetite, hematite, cassiterite, chlorite, quartz, galena, skarn garnet, uraninite, phosphates and scheelite (e.g., Courtney-Davies et al., 2019; Dare et al., 2014; Depiné et al., 2013; Emsbo et al., 2015; George et al., 2015; Guo et al., 2018; Li et al., 2018; Park et al., 2017; Rusk et al., 2011; Su et al., 2019; Wilkinson et al., 2015).

2.5. Biological and environmental applications

The range of bioimaging application by LA-ICP-MS is rapidly expanding, and the reader is referred to the recent reviews of Pozebon et al. (2017) and Fernández (2019) for a more comprehensive list. The technique has been applied to trace metal imaging of elemental and nanoparticle uptake in animal tissue (bone, hair, teeth and organs such as the brain, heart, kidneys etc.) and plant tissue (root, leaf, stems, seed etc.). These applications include (i) mapping the distribution of disease-relevant metals within the brain as age-related neurological disorders such as Alzheimer's and Parkinson's disease feature disrupted metal homeostasis (Hare et al., 2017), (ii) tracking metals (e.g. Pt, Ru and Cu) employed as metallodrug candidates for therapeutic exploitation (Moreno-Gordaliza et al., 2011), (iii) optimising treatments by imaging of the biodegradation of alloy implants in bone tissue (Draxler et al., 2015) and (iv) imaging mass cytometry by LA-ICP-MS – mapping metal isotope tags covalently bound to antigens and antibodies (e.g. Neumann

et al., 2020).

Tissue imaging has also been applied to investigate the role of trace metals in the function of cells. Approximately one third of all proteins require a metal atom or cofactor to function properly; some trace metallic elements (e.g. Mo, Cu, Fe, Zn, Co) are essential for human health, nutrition and plant growth, while other metals (e.g. Cd, Hg, Pb) are potentially toxic. Van Malderen et al. (2017b) investigated the spatial distribution of both micronutrients and toxic trace metals/metalloids in wheat and rye by LA-ICP-MS mapping with 3D reconstructions enabled by a serial sectioning approach (Fig. 3c). In addition to 3D elemental reconstructions employing serial sectioning or microtoming, bioimaging applications have been the catalyst for other developments in the field of LA-ICP-MS mapping. These include the development of low-dispersion (ultra-low dispersion) laser ablation cells for minimising signal smearing (Van Malderen et al., 2015) and considerations on how to avoid imaging artefacts (spectral skew) in low-dispersion cells when coupled to a sequential analyser such as an ICP-MS (Van Malderen et al., 2018). These advances are discussed in more detail in section 3.

LA-ICP-MS elemental imaging has also been applied to (paleo)environmental applications. These include mapping migratory and dietary transitions in modern and fossil organisms such as Sr-isotope distributions in fish otoliths (calcium carbonate 'ear stones') (Woodhead et al., 2007) to characterize natal stream signatures and the timing of subsequent migration, and Ba distributions in the teeth of modern-day human children and macaques and Middle Palaeolithic juvenile Neanderthals to constrain the dietary transition from the introduction of mother's milk through the weaning process (Austin et al., 2013). Paleoclimate applications include mapping B isotope variations in coralline algae for the investigation of ocean pH and temperature changes (Fietzke et al., 2015) and characterising seasonality in large benthic Paleogene foraminifera (Evans and Müller, 2013; Fig. 3d). Palaeochemistry studies employing LA-ICP-MS elemental mapping include characterising the depletion in Zn during the progressive breakdown of primary minerals in laterite soils (Suhr et al., 2018), elemental mapping of complex detrital pyrite cores in fluvial sequences immediately predating the Great Oxygenation Event which show that the Palaeoproterozoic atmosphere was devoid of any significant amount of free oxygen (Zhou et al., 2017) and mapping of deep sea Fe-Mn nodules which show how elemental maps resolve alternating periods of precipitation from variably intense hydrothermal input (Petrus et al., 2017; Fig. 3e) and how Fe-Mn micronodules are carriers of valuable metals (Co, Ni) and the REE + Y (Li et al., 2020).

3. Technical considerations

Section 2 highlighted the diverse range of applications that can be undertaken by LA-ICP-MS imaging. These applications can be broadly subdivided into two main groups – mapping of trace elements at the hundreds of ppm level (and below) which is not possible on conventional SEM-WDS or SEM–EDS systems, and isotope mapping (either isotopic tracing or U-Pb geochronology), section 4. The technical considerations required for these applications are discussed below.

3.1. Choice of instrumentation

Firstly, data reduction packages for producing LA-ICP-MS images typically require a laser log file that contains the time-stamped X-Y position of laser line scans for accurate registration with the time-resolved ICP-MS data. This has now become routine functionality on most modern laser ablation systems, and the most significant issue in laser ablation systems for elemental imaging is particle dispersion generated within the cell and the transfer tubing into the ICP-MS. The signal decline response from an individual laser pulse results in overlap of the pulse responses of sequential laser shots, resulting in smearing of signals such as when passing from a zone of high elemental concentration to a zone characterised by lower abundances of the same element(s).

Most modern laser ablation systems designed for geoscience applications are equipped with a two-volume cell (cf Müller et al., 2009), which typically have a single pulse response duration on the order of hundreds of ms to a second (Van Malderen et al., 2016). Approaches to further reducing the pulse duration involve minimizing aerosol dispersion in the cell and transport tubing. Recent advances in low dispersion laser ablation cells can now produce single pulse responses with a full width at 10% of the maximum peak intensity (FW0.1M) of c. 1 ms (Van Malderen et al., 2020) while also providing enhanced sensitivity as the analyte ions are less diluted during aerosol transport. The ultrarapid response provided by these small-volume, custom-built cells are particularly suited to coupling to simultaneous ICP-MS instruments such as an ICP-TOF-MS (Gundlach-Graham and Günther, 2016). An alternative approach to achieving a rapid pulse response is to take a conventional two-volume laser-ablation cell and replace the conventional polymer transport tubing to the ICP-MS torch interface with the short (c. 1 m) and narrow (internal diameter of c. 1 mm) transport tubing assembly of an ultrarapid-response cell (Van Malderen et al., 2016). Such rapid aerosol introduction systems are significantly cheaper than custom-built ultralow dispersion cells, while the large sample holder of the two-volume laser-ablation cell is maintained so multiple standards and unknowns can be accommodated. They provide single pulse response times of c. 20-35 ms (Van Malderen et al., 2018; Chew et al., 2019), and are becoming increasingly used in LA-ICP-MS imaging applications.

Single-collector ICP-MS systems employ a sequential mass analyser, and hence trace-element mapping requires a fast scanning ICP-MS instrument, typically a quadrupole ICP-MS or a sector-field single collector ICP-MS equipped with an Electric Sector Analyser (ESA). In a sector-field single collector mass spectrometer, mass jumps using an ESA are substantially faster than scanning by changing the magnetic field, but ESA peak jumps are typically restricted to < 40% of the total mass range. A time of flight (TOF) detector employs near-simultaneous detection and hence LA-ICP-TOF-MS is a promising tool as the entire elemental mass spectrum is recorded for each laser pulse; LA-ICP-TOF is discussed further in section 5.

High-precision isotopic ratio mapping experiments are hampered by the transient nature of laser ablation signals and ICP-MS multiplicative source noise (flicker). However, since flicker noise is a type of correlated noise, it may be minimized by recording isotopic data on all detectors simultaneously. LA-MC-ICP-MS offers true simultaneous detection and this approach has been applied to mapping B isotope variations in coralline algae with a $\delta^{11}B$ precision < 0.5‰ (section 2.5; Fietzke et al., 2015) using a grid of spots approach (cf section 4.2), mapping Sr-isotope distributions in fish otoliths with a $^{87}Sr/^{86}Sr$ ratio precision of < 100 ppm (section 2.5; Woodhead et al., 2007), and mapping Zn stable isotope tracers in rat organ tissue with a $^{67}Zn/^{64}Zn$ precision of c. 200 ppm (Urgast et al., 2012). All these experiments employed Faraday cups as they offer superior stability, linearity and ease of inter-calibration compared to ion counters. However, the electronic baseline noise of Faraday detector amplifiers (typically c. 100 mV on a Thermo Scientific™ Neptune) limits measurement precision, thus requiring larger spot sizes compared to ion counter detection. While the latest generation of 10^{13} Ω amplifiers offer significantly improved signal-to-noise ratios compared to conventional 10^{11} Ω amplifiers, they exhibit slower response and decay times (Kimura et al., 2016). Dynamic time-based (tau) correction can be applied to each amplifier and this approach works well for isotopic ratio determinations in homogenous geological materials such as volcanic glasses (Kimura et al., 2016). However, the response times of 10^{13} Ω amplifiers are unsuitable for rapid mapping of geological materials that exhibit significant zoning in elemental and / or isotopic ratios, such as U-Pb age mapping of zircon. Other challenges in LA-MC-ICP-MS mapping studies include inter-calibration of mixed Faraday/ion-counter setups, dynamic space charge effects and the limited dynamic range of MC detector arrays where concentrations vary substantially within an image, and a bias ('blind

time') on isotope precision in LA-MC-ICP-MS setups employing mixed detector arrays and highly transient signals produced by ultra-low dispersion cells (Craig et al., 2020).

3.2. Setting up an LA-ICP-MS mapping experiment

The following section considers how to set up a mapping experiment on a fast scanning, single-collector ICP-MS (e.g. a Q-ICP-MS or a sector-field single collector ICP-MS employing ESA peak jumping). Key issues addressed include the number of isotopes, selecting the appropriate dwell times, laser spot size, scan speed and repetition rate, and the problems of signal skew and aliasing.

Clearly, in a single-collector system the measurement precision on an individual isotope measurement decreases as the number of analytes increases, as the dwell time on each isotope represents a progressively smaller percentage of the total mass sweep time. However, mapping experiments (e.g. George et al., 2018; Petrus et al., 2017; Dare et al., 2014; Ulrich et al., 2009; Fig. 3e) show that it is possible to acquire over 20 elements (including the 14 naturally occurring lanthanides) in one analytical session, with some studies analysing significantly larger numbers of isotopes (e.g. > 50, Li et al., 2020). The alternative approach (remapping the same area multiple times with a smaller analyte list) can suffer from computational difficulties, as most LA-ICP-MS data reduction packages cannot undertake precise spatial registration and data extraction for multiple images from different sessions. Selecting dwell times for an individual isotope is normally dictated by the assumed abundance in the sample of an individual analyte. While smaller dwell times would seem advantageous for high-resolution mapping, very short dwell times are affected by increased readout noise and readout delays which become significant at sub-ms intervals. Longer dwell times have the advantage that a smaller fraction of total mass sweep is taken up by overhead and processing time, and can also reduce the temporal variation in signal intensity (beating) caused by pulsing of the laser in systems equipped with low dispersion cells.

The laser spot sizes, scan speeds and repetition rate of the applications described in section 2 are listed in Table 1. The laser fluences are not detailed but typically a fluence of 2 - 4 J/cm^2 is sufficient to ablate most geological matrices, bone material or teeth, while tissue imaging studies commonly employ laser fluences up to an order of magnitude lower (Hare et al., 2017). The laser spot size is application dependent and is chiefly determined by the assumed elemental abundances and the scale of the elemental variations (e.g. zoning in igneous phenocrysts or metamorphic porphyroblasts, or seasonal variations in biogenic carbonates). The most recent studies listed in Table 1 show that the spot sizes now employed typically range between 5-30 μm, even for elements at the ppb level (e.g. REE in olivine, Stead et al., 2017). Laser scan speeds typically range between 0.5 – 2X the laser beam size per second, although bioimaging applications (which investigate large mapped areas and often do not exhibit the micron-scale elemental variation characteristic of some geomaterials) have employed laser scan speeds as high as 10X the laser beam size per second (e.g. Van Malderen et al., 2017b). Such fast scan rates require high repetition rates to ensure that adjacent spots overlap. Extremely high (e.g. ≥ 100 Hz) repetition rates are becoming increasingly common in recent LA-ICP-MS imaging studies (Table 1), with repetition rates of 500 Hz now possible (Šala et al., 2020). While not all laser systems currently installed in geoscience laboratories are capable of running at such high repetition rates, such an approach offers several advantages in addition to enabling fast scanning. These include being able to employ smaller spot sizes than conventionally used for high-resolution imaging of low abundance elements, while running at high repetition rates in rapid response laser-ablation cells minimizes the temporal variation in signal intensity caused by pulsing of the laser as the signal will not return to background values at very high repetition rates.

In the following discussion of the spatial resolution of LA-ICP-MS maps, it is assumed for convenience that the mapped area is rectangular

(which is typical of the vast majority of studies) and the direction of laser stage translation is horizontal (i.e. along the x-axis of the map). The map is constructed as a series of adjacent horizonal lines of signal intensity data plotted *vs* time, with each mass spectrometer measurement represented by a pixel and the y-axis resolution represented by the laser spot size. Assuming an infinitely small spot size and zero dead volume in transporting the aerosol from the ablation site to the plasma torch (i.e. negligible dispersion), the theoretical resolution of a single pixel on the x-axis of the map is equal to the total cycle time × the scan speed. However, the laser spot must have sufficient area to surpass the detection limits of the analysed isotopes. This results in smearing of information due to both admixture sampling when the spot size is larger than sharp concentration gradients and the non-negligible pulse response. Ubide et al. (2015) show that features c. 75% the width of the spot size can be imaged using a conventional LA-ICP-MS two volume cell, while mathematical approaches based on deconvoluting the information contained in adjacent overlapping spots have been used to remove outliers (Paul et al., 2012) and to achieve sub-spot size resolution (e.g. Fox et al., 2017; Van Malderen et al., 2015). The lateral resolution can also be modelled theoretically once the ablation crater profiles and LA-ICP-MS profiles of single pulses are determined (Van Elteren et al., 2016).

The following guidelines are suggested for mapping experiments. Where possible we recommend employing high (e.g. ≥ 50 Hz) repetition rates to enable fast scan speeds, facilitate small spot sizes for high-resolution imaging of low abundance elements, and to minimize pulsing of the laser in low dispersion cells. On laser ablation systems where such fast repetition rates are not possible, some degree of signal smoothing must be employed and the scan speeds consequently need to be slower. Of critical importance is the interaction between the laser repetition rate and the total sweep cycle time (the sum of all the individual isotope dwell and settling times). One approach is a frequency matching approach, where the sweep cycle frequency (f_s) is set as a multiple of the laser repetition rate (f), i.e. $f = N \times f_s$, (Van Malderen et al., 2018). Another approach, involves detuning the frequency to avoid spectral skew artefacts by averaging signal intensities based on the least common multiple of sweep cycle frequency and laser repetition rate (Hattendorf et al., 2019). However, obtaining a stable response for each isotope by matching the sweep cycle frequency to a multiple of the repetition rate involves characterizing the width of the signal peak generated from a laser pulse on the sample and tailoring the key experimental parameters accordingly (Van Malderen et al., 2018). Characterization of the single pulse response is key, as it enables equations to be derived to calculate the ideal spot size, laser repetition rate, dwell times and total sweep cycle time for a specific LA-ICP-MS system (Van Elteren et al., 2019). Additionally, while matching the sweep cycle frequency to a multiple of the repetition rate works well for a very small analyte list, long multi-element LA-ICP-MS mapping sessions of geomaterials are prone to very minor drift in synchronization of the laser repetition rate and the sweep cycle sampling frequency (i.e., very minor under- or oversampling). This results in an extremely low-frequency aliased waveform in the resultant signal intensities which causes highly inaccurate elemental signals (i.e. false concentration gradients) from both maps and reference glass line scans. Improvements in the hardware and software controlling the interface between the LA system and the ICP-MS may in future allows precise synchronization between individual laser pulses and the quadrupole total sweep cycle frequency.

Fig. 4a illustrates such a low-frequency waveform produced by temporal aliasing, resulting in a Moiré interference pattern in the resulting image (*cf* Van Elteren et al., 2018). This image was produced on a system with an aerosol rapid introduction system with a response duration to a single pulse of 35 ms (FW0.01M, the full peak width of the signal at 1% of the maximum peak intensity). Signal smoothing was thus employed, giving a response duration of c. 1 s for a single pulse. Even with signal smoothing and a relatively high laser repetition rate (f
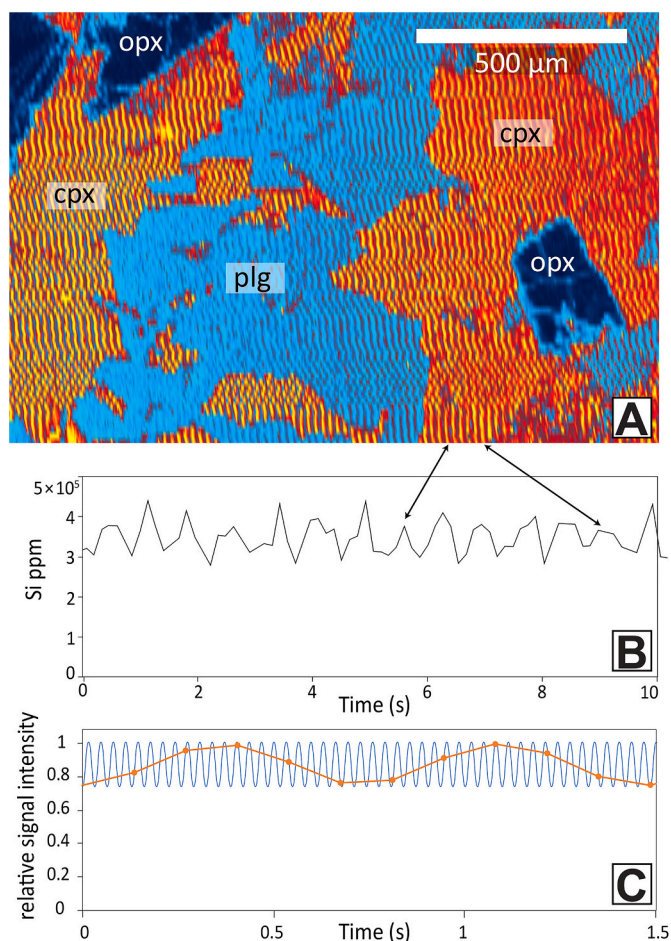
Fig. 4. A) low-frequency waveform produced by temporal aliasing, resulting in a Moiré interference pattern in the resulting image (an Si concentration map of a basalt where cpx = clinopyroxene, opx = orthopyroxene and plg = plagioclase). The image was acquired with a relatively high laser repetition rate (f = 31 Hz) and a sweep cycle frequency of f_s = 7.407 Hz (total sweep cycle = 135 ms). B) Low-frequency periodic desynchronization in the time-resolved Si ppm signal on NIST 612 reference glass from the same experiment with the resultant aliased waveform yielding a measured frequency (f_{alias}) of 1.376 Hz (λ = 727 ms). The aliased waveform in the cpx in A) has an identical wavelength. C) Modelled signal intensity (blue curve) of an individual laser pulse (a sine function with f = 31 Hz) and an amplitude of 25% of the peak intensity because the signal does not return to background due to signal smoothing. Sampling this modelled signal every 135 ms produces the orange aliased waveform with a measured frequency (f_{alias}) of 1.371 Hz (λ = 729 ms).

f = 31 Hz), line scans on the NIST 612 reference glass at the start and end of the session show evidence for low-frequency periodic desynchronization (Fig. 4b), with the resultant aliased waveform yielding a measured frequency (f_{alias}) of 1.376 Hz (λ = 727 ms). Modelling the signal intensity of an individual laser pulse as a sine function with f = 31 Hz and an amplitude of 25% of the peak signal (as the signal does not return to background at this repetition rate due to signal smoothing), and then sampling the modelled signal using the sweep cycle frequency (f_s = 7.407 Hz) every 135 ms results in an aliased waveform (Fig. 4c) with a measured frequency (f_{alias}) of 1.371 Hz (λ = 729 ms). This is identical to the theoretical frequency of the aliased waveform (f_{alias} = 1.370 Hz; λ = 729 ms) calculated from the equation f_{alias} = min($| f - N \times f_s |$), where $N \in \mathbb{N}$ (Van Malderen et al., 2018).

These data demonstrate that even with significant signal smoothing, a moderately high laser repetition rate and a total sweep cycle several times longer than the laser repetition rate, deleterious Moiré interference patterns can be seen in images. Several approaches can be

employed to minimize this temporal aliasing effect. Increasing the extent of signal smoothing results in smearing of signals and hence increasing the laser repetition rate is preferred as it decreases the amplitude of the resultant aliased waveform. Knowledge of the total sweep cycle time (as opposed to the total dwell time) is key. This enables the total sweep cycle frequency (f_s) to be set as multiple of the laser repetition rate if the ICP-MS can maintain perfect synchronization of the sweep cycle frequency with the repetition rate over the course of a long analytical session, or adjusting the laser repetition rate (f) so that f_{alias} = min($| f - N \times f_s |$) results in a high-frequency waveform with a wavelength of twice the duty cycle which would either not be noticeable on a large mapped area (particularly if the amplitude of the aliased waveform is small), or is easily smoothed post data acquisition. In all cases, we recommend starting the experiment and examining the live, time-resolved signal intensities of several isotopes on reference glass line scans at the start of the session to check for temporal aliasing effects.

3.3. Data visualization and extraction tools

The advent of LA-ICP-MS imaging has led to the development of dedicated data reduction and image processing packages, as detailed in section 1.2. Many of these software packages offer some additional features such as the ability to construct elemental concentration profiles across maps or visualize correlations between the signal intensity of isotopes. However, the latest advances in high-speed and high-resolution mapping have led to the development of a suite of packages with enhanced functionality which are of particular relevance to the geosciences, three of which are described below. These tools have significantly furthered visualization, interrogation and extraction of quantitative data from LA-ICP-MS maps, and may result in LA-ICP-MS imaging superseding conventional spot analysis as the routine approach to many LA-ICP-MS applications in the geosciences.

XMapTools (Lanari et al., 2014) is a MATLAB©-based set of modules originally designed to process, standardise and interrogate EPMA images for petrological studies. Functionality includes a range of image and data processing modules such as colour enhancement tools, line profile generation, binary and ternary compositional plots, phase identification and local bulk composition calculations for P-T calculations. An extension to XMapTools was introduced by Raimondo et al. (2017) so that it can import LA-ICP-MS data to visualise and interpret compositional zoning patterns in metamorphic porphyroblasts, along with modules to generate multi-element RGB image stacks, trace element ratio calculations, and normalised REE diagrams. Although the software does not reduce or standardise LA-ICP-MS data (maps must be imported as quantified ppm data with each element presented in a numerical matrix format), additional processing modules are being developed for XMapTools and it is frequently updated.

The HDF-based Image Processing (HDIP) software (Teledyne CETAC Technologies, 2020) places specific emphasis on processing and visualising LA-ICP-MS imaging data in 2D and 3D. HDIP can accept data from a broad range of LA-ICP-MS instrumentation as well as from other microscopy techniques, and all elemental and optical images can be layered on top of each other and aligned. It is equipped with several sophisticated features, including multi-standard external calibration; an AutoPilot feature which enables fully autonomous data reduction through to the generation of publication-quality images; the LaOptimize tool which based on the peak profile of a single laser shot can find the optimum imaging parameters to correct for the blurring effects caused by the pulse response; a Channel Calculator which allows user-defined formulas to be applied to different mass channels and a suite of image editing tools.

Iolite (Woodhead et al., 2007; Hellstrom et al., 2008; Paton et al., 2011) is a software package developed for mass spectrometric data reduction (ICP-MS and TIMS). Similar to HDIP it can accept data from a broad range of LA-ICP-MS instrumentation. It was originally developed

as a set of procedures for Igor Pro (http://www.wavemetrics.com), a platform for scientific graphing, data analysis and image processing of time series data, but the latest version (v4) runs as a standalone software package. Iolite is capable of processing very large datasets (e.g. multi-hour sessions of laser ablation data) with a strong emphasis on viewing and editing data in graphical form as plots of signal intensity, isotopic ratios or elemental ratios versus time. Data reduction of the input channels is undertaken by one of many modules (referred to as a "Data Reduction Scheme" or "DRS") each of which is stored in a discrete, user-editable file. There is a growing number of DRSs that are either supplied with Iolite or are produced by independent developers. These DRSs undertake diverse functions such as baseline subtraction, correcting for instrumental drift, interpolating mass bias, calculating standardised trace-element abundances or downhole elemental fractionation in U-Pb geochronology. Imaging features includes the Cellspace and Monocle plug-ins, which along with stacked image functionality and 3D viewing are now built into Iolite v4. Cellspace (Paul et al., 2012) displays time-resolved isotopic data versus ablation position (i.e., spatially). These data can be plotted over a variety of other spatially registered microscopy images enabling visualization in a petrographic context, while the Cellspace approach also enables deconvolution of the information contained in adjacent overlapping spots to remove outliers (Paul et al., 2012). Monocle (Petrus et al., 2017; Fig. 3e) is an extremely powerful interrogation tool for 2D LA-ICP-MS element and isotope maps. It enables inspection of map data using an adjustable 'loupe' that can be moved across the map in conjunction with a series of live inspector tools (histograms and probability density plots; Fig. 3e) of element concentration, ratio or U-Pb age. Live graphs of normalised REE concentrations (Fig. 3e) or U-Pb concordia are also available depending on the dataset. A particularly powerful feature is the ability to define and obtain statistics for user-defined regions of interest (ROIs). These ROIs can be defined either by drawing polygons over irregular zones of similar chemistry, by growing a ROI from a 'seed' where the data distribution in the seed is used to find adjacent pixels that are within a user-defined statistical boundary, or by defining numerical criteria (e.g. Rb < 0.3 ppm; Ca > 35 wt%; Mg/Ca < 0.004). The application of Monocle to image-based U-Pb geochronology is discussed further in section 4; much of the image processing functionality of Monocle is also now available in HDIP.

4. Geochronological applications

4.1. LA-ICP-MS imaging as a guiding tool for spot ablation geochronology

Many *in situ* geochronological approaches employ initial textural characterization of the target phase prior to dating by a microbeam technique. Examples include U-(Th)-Pb dating of complex, polyphase zircon (section 4.2) or monazite (section 4.3), where discrete age domains are often linked with specific rock-forming processes and their physical conditions (i.e. petrochronology, Engi et al., 2017). Initial textural characterization of such accessory phases commonly employs CL imaging, and particularly in the case of monazite, SEM-EDS or -WDS mapping to link monazite growth domains with specific mineral assemblages and reactions (section 4.3). Sections 4.2 - 4.4 below primarily show how LA-ICP-MS trace-element imaging can be integrated with simultaneous U-Pb geochronology imaging.

LA-ICP-MS trace-element imaging has also been employed as a guiding tool to aid U-Pb dating by static *in situ* microbeam techniques or micro-drilling followed by isotope dilution (ID)-TIMS analysis, particularly when U or petrogenetically important trace elements are present at concentrations below the detection limits of SEM-EDS or -WDS mapping. LA-ICP-MS trace-element imaging has been applied as an initial characterization tool in U-Pb and U-series geochronology of carbonate minerals, which typically exhibit very low U concentrations (c. 10 ppb to 10 ppm U, Roberts et al., 2020; section 4.4) compared with traditional U-bearing accessory minerals. Precision in U-Pb and U-

series geochronology of carbonate minerals is thus highly dependent on detecting high-U domains of pristine primary carbonate, but unlike zircon, CL intensity in carbonate phases typically cannot be used as a proxy for U concentration (Mn^{2+} is the most dominant luminescence activator and Fe^{2+} is the dominant luminescence quencher). LA-ICP-MS concentration profiles (i.e. line scans) have been used to rapidly characterize U and Th distributions in tooth enamel and dentine as a precursor to ID U-series dating (Eggins et al., 2003) and also in direct U-series dating by LA-MC-ICP-MS of speleothems, molluscs, bones and teeth (e.g. Eggins et al., 2005; Woodhead et al., 2016). LA-ICP-MS trace element imaging is also commonly employed in U-Pb LA-ICP-MS carbonate dating studies employing static spot ablations (e.g. Roberts and Walker, 2016; Roberts et al., 2020 and references therein) to target, refine, and interpret U-Pb age data, including detecting portions of sample which exhibit sufficient spread in $^{238}U/^{204}Pb$ ratio (μ) and mapping of trace elements diagnostic of primary carbonate to exclude zones of potential alteration or detrital contamination (*cf* section 4.4).

4.2. Zircon

Existing approaches to producing accessory mineral LA-ICP-MS U-Pb age (zircon; Gehrels et al., 2008) or combined U-Pb age and trace element maps (titanite, Spencer et al., 2013, Timms et al., 2020; monazite, Horton et al., 2016 and Woodhead et al., 2016) have typically employed contouring or kriging of spot ablation data. The need for contouring can be avoided using a contiguous grid of spots; this approach was adopted by Kelly et al. (2017) who undertook LA-ICP-MS trace element (Al, Si, P, Fe, Sr, Y + REE, Hf, Th and U) mapping of zircon using 7 μm diameter spot ablations. However, LA-ICP-MS U-Pb and / or trace element imaging using a spot ablation approach is time consuming, typically requiring several hours analysis per grain.

Zircon is able to preserve multiple events within individual zircon grains, such as magmatic or high-grade metamorphic zircons with core-rim structures and Pb mobility episodes not linked to discrete crystallization events (Pb loss, incorporation of common Pb, high-temperature Pb mobilization). This makes it an attractive target for LA-ICP-MS U-Pb age mapping studies to constrain fine-scale processes affecting the U-Pb zircon systematics. Chew et al. (2017) present a suite of LA-ICP-MS U-Pb age, U, Th and Th/U ratio maps (along with CL and Raman intensity images) of zircons from Palaeozoic syn-tectonic leucosomes and post-tectonic granitoids intruding metasedimentary rocks in the Eastern Cordillera of Peru. Zircons in these rocks are coarse-grained (typically c. 200×100 μm^2) and have clearly defined cores and rims based on CL imaging and earlier *in situ* U-Pb SIMS and LA-ICP-MS geochronology studies (Chew et al., 2007).

Zircon rim concordia ages derived from the U-Pb age maps are consistent with the independent geochronology constraints, while secondary-standard data typically reproduced within 1% of their published crystallization ages (Chew et al., 2017). The secondary standard data yielded weighted average $^{206}Pb/^{238}U$ age precisions (for an individual crystal) of between 0.5 and 1% (2 RSD) for Palaeozoic reference materials and between 1.5 and 2% (2 RSD) for Cenozoic age standards. These quoted weighted average $^{206}Pb/^{238}U$ age precisions are derived from c. 10 rasters on the same grain; the precision on an individual raster is between 2 and 4% (2 RSD) for Palaeozoic reference materials and between 4 and 8% (2 RSD) for Cenozoic age standards.

Age accuracy was therefore not affected by laser-induced elemental fractionation between the different zircon samples at the high (45 Hz) ablation rates employed (analytical setup is detailed in Supplementary Table 1). The zircon in Fig. 5 is from a c. 480 Ma syn-tectonic leucosome (grain 823 from sample DC 05/5-7; Chew et al., 2017), and exhibits a thin (10 to 30 μm) CL-dark rim with idiomorphic zoning, surrounding a large inherited magmatic core (zoned and CL-bright) constituting the bulk of the zircon crystal. There is a clear correlation between U concentration and the CL image (CL dark = high U; CL bright = low U; Fig. 5a, b). The $^{206}Pb-^{238}U$ map (Fig. 5e) and the
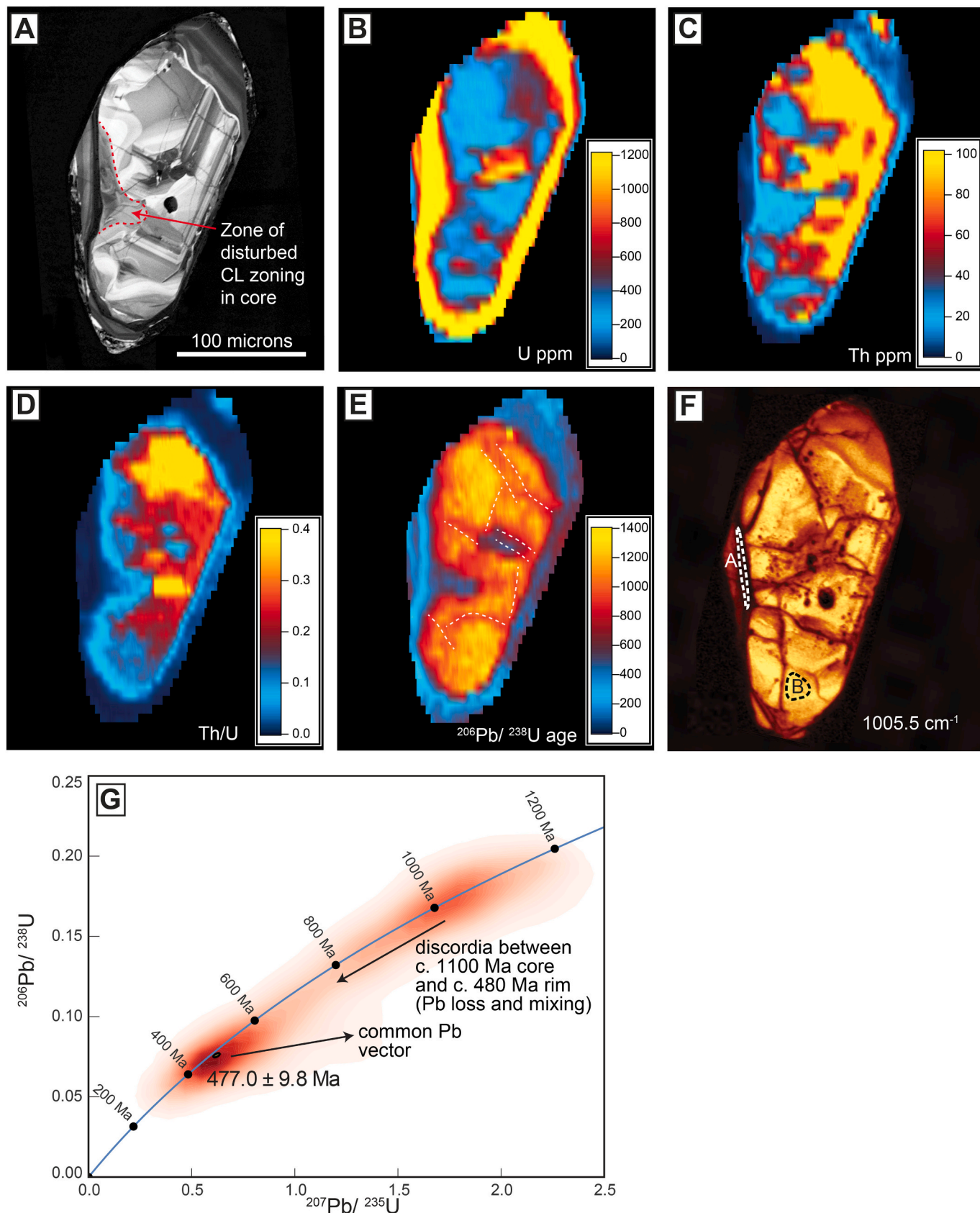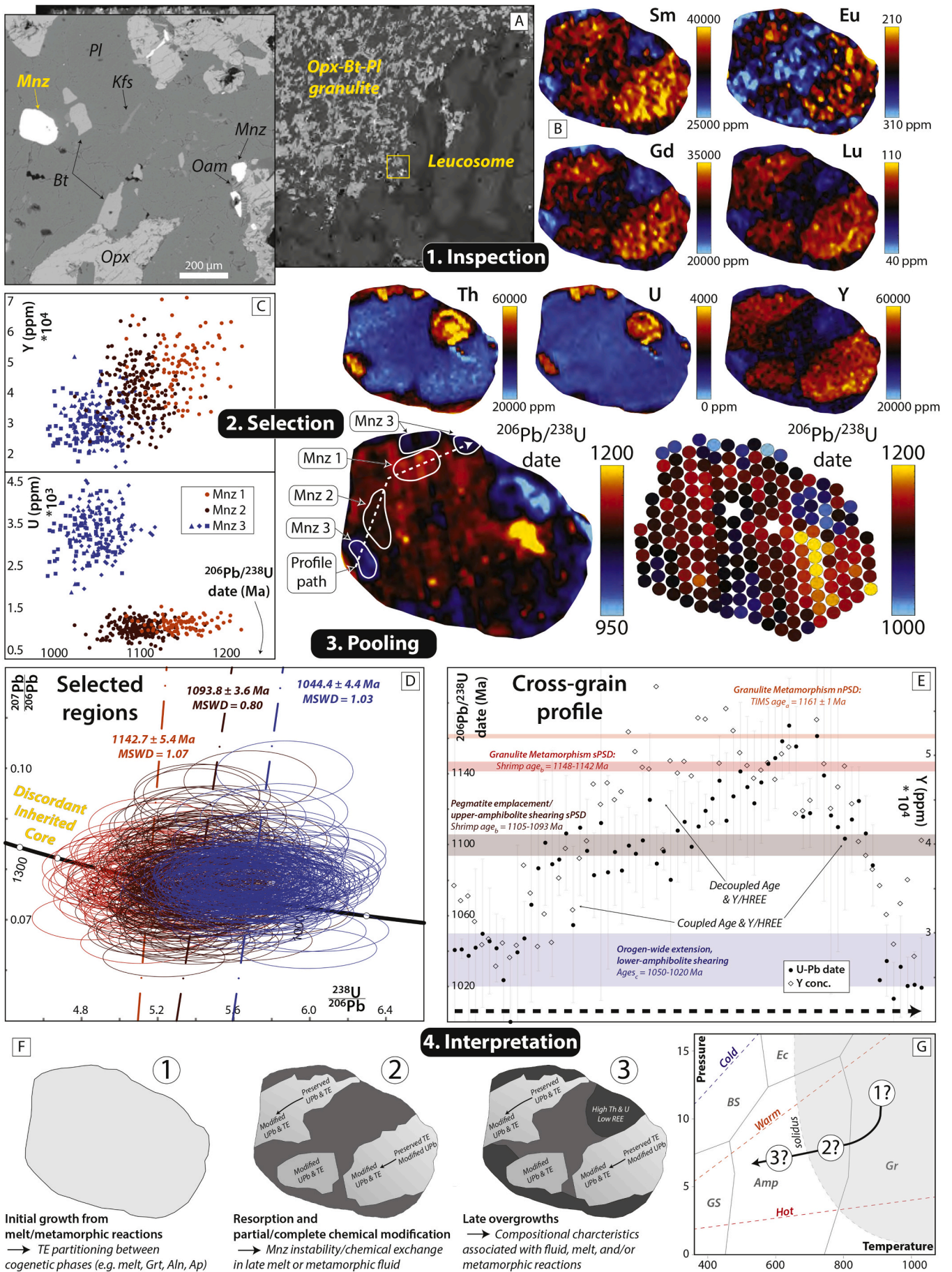
Fig. 5. Zircon 823 from a syn-tectonic leucosome from the study of Chew et al. (2017). A) CL image. B–E) LA-ICP-MS U ppm, Th ppm, Th/U ratio and $^{206}Pb/^{238}U$ age image maps. The dashed white lines on the $^{206}Pb/^{238}U$ age image map denote fractures traced directly off the CL image which spatially correlate with domains of Pb loss. F) Raman peak intensity map at the 1005.5 cm-1 band. G) Two-dimensional kernel density estimates from $4 \times 4 \mu m$ "data" blocks plotted in the Wetherill concordia space. Modified from Chew et al. (2017).

Figure panels:

A — BSE images showing Mnz, Pl, Kfs, Bt, Opx, Oam, Opx-Bt-Pl granulite, Leucosome. Scale bar 200 μm.

B — Trace element maps: Sm (25000–40000 ppm), Eu (210–310 ppm), Gd (20000–35000 ppm), Lu (40–110 ppm), Th (20000–60000 ppm), U (0–4000 ppm), Y (20000–60000 ppm).

1. Inspection

C — **2. Selection**
Y (ppm) *10^4 vs ^206Pb/^238U date; U (ppm) *10^3 vs ^206Pb/^238U date (Ma)
Legend: Mnz 1, Mnz 2, Mnz 3

^206Pb/^238U date maps (1200–950; 1200–1000), regions: Mnz 3, Mnz 1, Mnz 2, Mnz 3, Profile path

3. Pooling

D — Selected regions
207Pb/206Pb vs 238U/206Pb
1093.8 ± 3.6 Ma, MSWD = 0.80
1044.4 ± 4.4 Ma, MSWD = 1.03
1142.7 ± 5.4 Ma, MSWD = 1.07
Discordant Inherited Core, 1300, 1000

E — Cross-grain profile
^206Pb/^238U date (Ma) vs Y (ppm) *10^4
Granulite Metamorphism nPSD: TIMS age_a = 1161 ± 1 Ma
Granulite Metamorphism sPSD: Shrimp age_b = 1148–1142 Ma
Pegmatite emplacement/upper-amphibolite shearing sPSD Shrimp age_b = 1105–1093 Ma
Decoupled Age & Y/HREE
Coupled Age & Y/HREE
Orogen-wide extension, lower-amphibolite shearing Ages_c = 1050–1020 Ma
Legend: • U-Pb date, ◇ Y conc.

4. Interpretation

F —
① Initial growth from melt/metamorphic reactions
→ TE partitioning between cogenetic phases (e.g. melt, Grt, Aln, Ap)

② Resorption and partial/complete chemical modification
→ Mnz instability/chemical exchange in late melt or metamorphic fluid
(Preserved UPb & TE, Modified UPb & TE, Preserved TE Modified UPb)

③ Late overgrowths
→ Compositional charcteristics associated with fluid, melt, and/or metamorphic reactions
(High Th & U Low REE)

G — Pressure vs Temperature
Cold, Warm, Hot, solidus, Ec, BS, GS, Amp, Gr
1?, 2?, 3?

(caption on next page)

Fig. 6. LA-ICP-MS trace element and U-Pb geochronology mapping of complex monazite. A) BSE images of the microstructural setting of the analysed monazite grain (yellow label), showing its position along the boundary between the host Opx-Bt-Pl granulite layer and adjacent Pl-Kfs-Qtz leucosome. B) False-color LA(SS)-MC-Q-ICP-MS line scan maps of Y, REE, Th, U, and $^{206}Pb/^{238}U$ age, as well as $^{206}Pb/^{238}U$ age map from subsequent spot analysis by same LA(SS)-MC-Q-ICP-MS setup. Note locations of representative regions and line profile selected for pooled data analysis shown in adjacent plots. C) Bivariate plot of Y and U concentration *vs* $^{206}Pb/^{238}U$ date, calculated for each pixel within the regions delineated in B. D) Tera-Wasserburg Concordia diagram plotting calculated ratios for each pixel within the regions delineated in B. An arbitrary 5% 2SE uncertainty is assigned to each data point, yielding an MSWD ~1 on the intercept dates for each population. Free regression lines following a near-vertical array of $^{207}Pb/^{206}Pb$ for each population were used to model minor systematic overdispersion. We infer the slight overdispersion to be an analytical or data-processing artefact, potentially resulting from the difference in signal response time (*cf* section 3.1) between ^{207}Pb (10^{12} Ω amplifier) and ^{206}Pb (10^{11} Ω amplifier), as opposed to common Pb or mixing with older age components. Identical concordant dates can be obtained for each population assuming a higher uncertainty in the individual $^{207}Pb/^{206}Pb$ (i.e. c. 10%). E) Y concentration and $^{206}Pb/^{238}U$ date for 10 μm² bins along the cross-grain profile delineated in B. Coloured bands indicate regional geochronological constraints from the literature, correlated with domains identified in monazite map. References to previous geochronological data: a – Van Breemen et al. (1986); b – Marsh et al. (2012); c – Rivers (2012 and references therein). F) Schematic diagram showing a generalized petrogenetic process interpretation for the defined zones within the analysed monazite grain. G) Inferred P-T path of the analysed granulite sample (GB97J) with timing constraints hypothetically linked to defined monazite compositional types and inferred petrogenetic process as shown in F. Metamorphic facies: GS – greenschist, Amp – amphibolite, Gr – granulite, BS – blueschist, Ec – eclogite.

Raman peak intensity map (at the 1005.5 cm^{-1} band; Fig. 5f) also identify core-rim relationships and additional internal structure. Fractures on the CL image spatially correlate with domains of Pb loss on the $^{206}Pb/^{238}U$ image map (Fig. 5e), while the Raman peak intensity map shows a dark zone of metamict zircon (zone 'A' on Fig. 5f which contains up to 7,500 ppm U on Fig. 5b) with low intensity and broadening of the $\nu 3$ SiO$_4$ band (not illustrated).

However, the Th distribution (particularly in the core) is highly complex (Fig. 5c), as is the resultant Th/U map (Fig. 5d). The zircon rims on the CL images are characterised by extremely low Th/U values of c. 0.02. The oldest concordant portions of the core (c. 1.1 Ga) are associated with the highest Th/U ratios (up to 0.4) and lowest U contents and are mantled by an outer portion of the core which is partially age reset and exhibits significantly lower Th/U ratios (c. 0.1) and higher U concentrations. U-Pb age resetting in the core likely resulted from Pb-loss from the higher U outer domain facilitated by fractures and metamictisation. Conventional spot analyses in the core of this polyphase zircon would likely result in a complex mixed age signal compromised by Pb loss. This is shown by 2D kernel density estimates of 4×4 μm "data" blocks sampled from the zircon and plotted in the Wetherill concordia space which define discordia mixing lines between the c. 480 Ma and c. 1.1 Ga age components and also a common Pb vector (Fig. 5g). Additionally, the significantly greater penetration depth of LA-ICP-MS spot ablations (typically 10 to 20 mm) would result in complex mixed age signals which would be even harder to relate to the surface imaging. The technique provides spatially constrained U-Pb age data directly relatable to other surface imaging techniques (and with the LA-ICP-MS U, Th and Th/U ratio images) which makes interpretation significantly more robust. Other elements (e.g. Fe, Sr, Li, REE, Hf), which may also yield additional petrogenetic information, can easily be added to the analytical protocol. The approach is easily modified for other high U/Pb accessory mineral phases (e.g. monazite; section 4.3) and to U-bearing phases that contain common Pb (e.g. carbonate, section 4.4). Other applications include imaging complex polyphase zircons and extracting data from polygons of isochronous areas (e.g. using Monocle; Petrus et al., 2017), correlating zones of Pb loss with high U; and characterising the U-Pb systematics of key samples for U-Pb TIMS dating.

4.3. Monazite

Along with zircon, monazite is the most common U-Th-Pb geochronometer utilized for precise dating of high-temperature processes in Earth's crust (e.g. melt crystallization and metamorphism), owing to the slow volume diffusion of most elements and negligible initial Pb, while its high Th and U abundances facilitate small ablation volumes. Additionally, the reactive behaviour of monazite in the presence of magmatic, metamorphic, and hydrothermal fluids facilitates recording the timing and conditions of multiple geologic processes that have affected a given volume of rock (Engi, 2017). Over the past two decades

considerable effort has been directed toward identifying geochemical linkages between monazite growth and specific mineral assemblages or geological conditions and modelling the associated phase equilibria relations (e.g. Pyle and Spear, 2003; Spear and Pyle, 2010; Yakymchuk et al., 2017). Given the likelihood of internal compositional heterogeneity within individual monazite grains, integrating petrological information with quantitative time constraints requires analysis of both the U-Th-Pb and trace element composition of identifiable monazite domains by *in situ* methods, yielding a radiometric date that can be linked with a specific petrological process (i.e. petrochronology; Williams et al., 2007, 2017; Kylander-Clark et al., 2013; Engi, 2017; Hetherington et al., 2017). Traditionally, initial textural characterization of target monazite was accomplished by high-contrast BSE imaging or (preferably) element mapping by EPMA; however, advances in LA-ICP-MS instrumentation and methodology have enabled acquisition of all the required compositional and age information at high spatial resolution (approaching that of SEM-WDS) through LA-ICP-MS elemental imaging.

In this section, we present a newly acquired dataset to demonstrate the potential of LA-ICP-MS mapping to quantitatively distinguish multiple internal domains that record episodes of monazite growth, dissolution, and (apparent) compositional modification. A ca. 200 μm diameter monazite grain located along a mesosome-leucosome boundary (Fig. 6a; Sample GB97J of Marsh and Stockli, 2015) within a polymetamorphic granulite terrane from the western Grenville Province (Ontario, Canada) was selected for analysis by LA, utilizing a split-stream configuration with simultaneous measurement of U-Th-Pb isotopes on a MC-ICP-MS and trace elements on a Q-ICP-MS, hereafter referred to as LA(SS)-MC-Q-ICP-MS (analytical setup is detailed in Supplementary Table 1). An initial line scan map was followed by a grid of conventional (static) 10 μm spots over the same area and with the same LA(SS)-MC-Q-ICP-MS instrumental setup, so that data accuracy could be compared between the two methods.

First-order inspection of the elemental (Y, REE, Th, and U) and U-Pb age maps enables definition of three general compositional types (Mnz 1, 2, & 3), the boundaries between which can be sharp or gradational and for some elements vary in position (Fig. 6b). Mnz 1 is defined as a Y-REE-rich, Th- and U-poor zone comprising three separate domains in the grain interior and yields the oldest U-Pb dates (outside of the discordant > 1200 Ma patch inferred as inherited/detrital). Mnz 2 has variably lower Y, M-HREE (especially Eu), and Th and slightly higher U, comprising most of the central portion of the grain, and yields intermediate U-Pb dates. Finally, distinct Y-REE-poor, Th and U-rich zones along the outer portions of the grain comprise Mnz 3, and yield the youngest U-Pb dates. U-Pb dates obtained from the line scan map are largely consistent with those obtained from the subsequent spot analyses. Trace element concentrations determined from the line scan and spot LA(SS)-MC-Q-ICP-MS methods are indistinguishable (not shown).

Selecting representative regions for each compositional type within the data processing software (Iolite 4) enables extraction of calculated
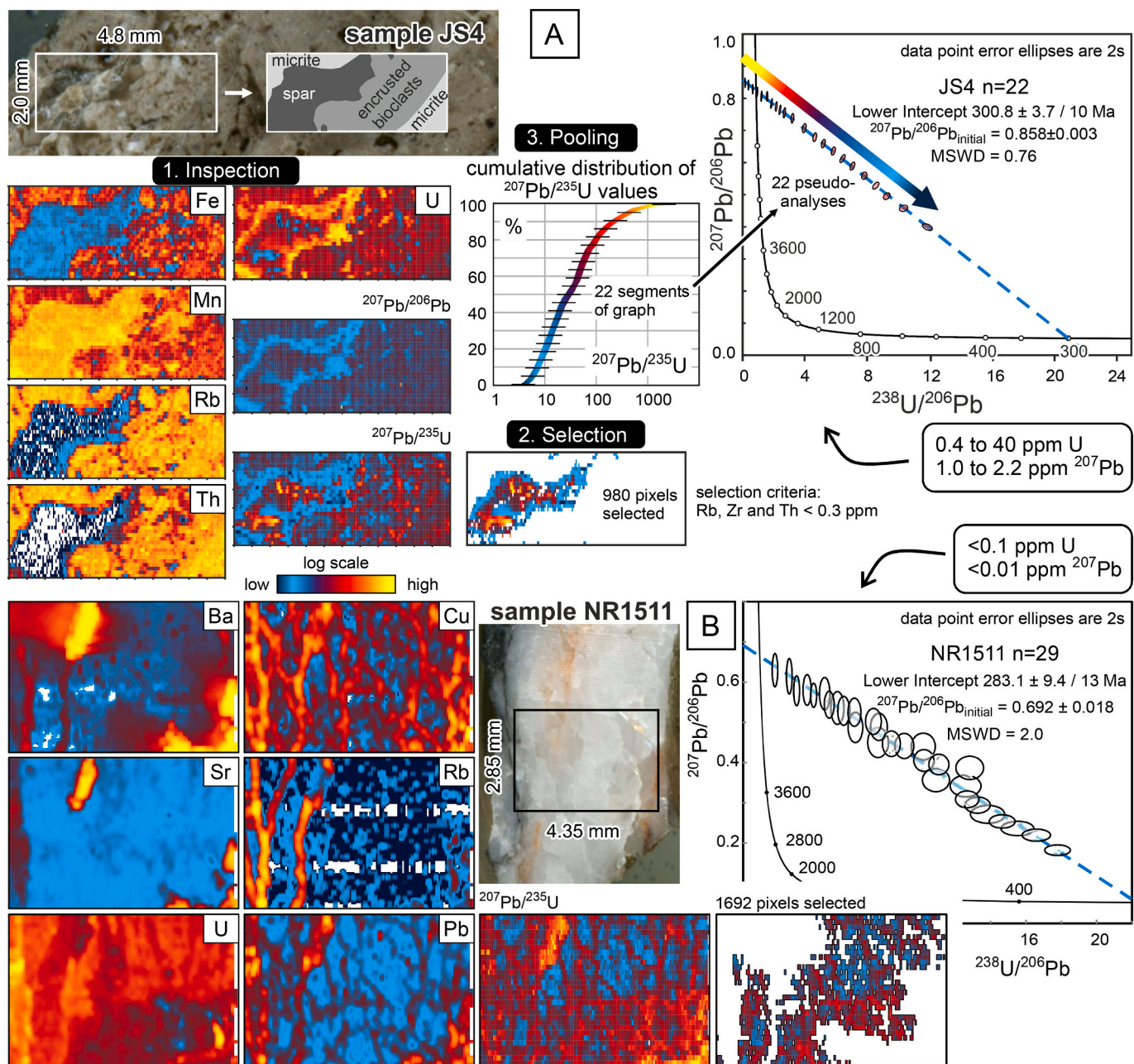
Fig. 7. LA-ICP-MS carbonate U-Pb geochronology using an image-based approach. A) Element and isotope ratio maps compiled and inspected to identify potentially different genetic domains. Suitable criteria (here Rb, Zr and Th < 0.3ppm; concentrations determined using NIST614 glass as a primary trace element reference material) were applied to isolate a domain (here calcite spar) that is likely homogeneous in age. The element and isotope ratio data corresponding to the selected pixels were pooled into 22 pseudo-analyses using an isotope ratio resembling the parent/daughter ratio (here the $^{207}Pb/^{235}U$ ratio) to retrieve the largest possible spread on concordia and isochron plots. Modified from Drost et al. (2018). B) Typical low U calcite sample from a vein with complex alteration patterns. The data were filtered to target the least altered domain for age determination and the selected pixels were pooled into 29 pseudo-analyses. Modified from Roberts et al. (2020).

concentration values, ratios, and dates for each pixel, such that compositional and age variables can be plotted or pooled for calculation of population statistics. The monazite types defined from visual inspection show clear relationships between U-Pb date and composition (Fig. 6c) and yield three distinct Concordia intercept dates with precision equivalent to traditional in-situ spot analyses (i.e. < 1% 2σ; 5% 2SE assumed for each data point; Fig. 6d). A profile across all three compositional types, with values and uncertainties calculated from 10 μm² bins, also shows distinct age domains with individual dates largely outside 2SE uncertainty from each other (Fig. 6e).

The dates from each compositionally distinct domain correspond

with established regional and local metamorphic events, as determined by previous zircon U-Pb analyses by TIMS, SHRIMP, and LA-SF-ICP-MS analyses. The 1143 ± 5 Ma date for Mnz 1 corresponds with the U-Pb ages assigned to peak granulite-facies metamorphism, with the 1094 ± 5 Ma date for Mnz 2 corresponding with the timing of pegmatite emplacement and local amphibolite-facies shearing (Marsh et al., 2012). The 1044 ± 4 Ma date for Mnz 3 corresponds with the widespread late-orogenic extension observed across the western Grenville Province (Rivers, 2012), which importantly has not been identified in numerous analyses of zircon from this area. Thus, the data from LA(SS)-MC-Q-ICP-MS mapping of a single monazite grain provides a

near complete record of tectono-metamorphic events affecting the region. Furthermore, the integrated spatial, compositional (TEs), and geochronological mapping data enable numerous process-oriented petrological research questions to be addressed (Fig. 6f & g).

4.4. Carbonate

Uranium-lead geochronology of the processes involved in the formation of calcite and other carbonate minerals (e.g. calcite veins and slickensides, hydrothermal and ore deposit carbonates, sedimentary limestone deposits, diagenetic carbonate cements, dolomitization, biogenic carbonate, speleothems) has become increasingly popular in recent years due to the increased precision and availability of LA-ICP-MS systems. The approach gives unique insights into the timing of a suite of geological processes which have been hitherto challenging to constrain. Detailed reviews on U-Pb carbonate geochronology were given by Jahn et al. (1994), Rasbury and Cole (2009) and Roberts et al. (2020), while the strategy, analytical protocol and data processing routines for image-based LA-ICP-MS U-Pb carbonate dating are described in Drost et al. (2018). The major challenges in U-Pb carbonate geochronology are typically very low U concentrations and associated limited ingrowth of radiogenic Pb, appreciable common Pb and the potential for genetically complex mineral assemblages. Nevertheless successful age determination is possible when certain requirements are met: (i) a closed U-Pb system (i.e. absence of U and/or Pb mobility post formation), (ii) a homogeneous initial Pb composition (i.e. common Pb must be represented by a single, authigenic component) and (iii) a sufficient spread in $^{238}U/^{204}Pb$ ratio (μ) to allow for a well constrained regression of data points. The superior spatial resolution of LA-based U-Pb carbonate dating compared to ID-TIMS U-Pb analysis (where sampling is usually undertaken by micro-drilling) offers distinct advantages in many samples in achieving a sufficient spread in $^{238}U/^{204}Pb$ ratio (Woodhead and Petrus, 2019).

Image-based LA-ICP-MS U-Pb carbonate dating allows identification of domains that are potentially homogeneous in origin and age by compilation and inspection of maps of characteristic major and trace elements, typically following petrographic characterization (e.g. by optical microscopy or CL). Major elements (e.g., Mg, Ca, Sr, Mn, Fe, Ba) assist in revealing potential changes in carbonate mineralogy or mineral transformations, while minor and trace elements help detect the presence of detrital material (e.g., Ga, Rb, Zr, Th) or migration and redistribution of elements during post-formational fluid activity such as diagenesis, deformation or hydrothermal overprinting (e.g., Mg, V, Mn, Cu, Rb, Sr, U). Depending on the available instrumentation, these elemental maps can either be used as a guide for spot analyses (see section 4.1) or can be acquired simultaneously along with U, Th and Pb isotope data by LA-ICP-Q-MS as detailed below.

Fig. 7 shows two examples of image-based U-Pb carbonate geochronology where inspection of element and isotope ratio maps led to definition of selection criteria to target pixels that likely correspond to the same genetic domain. The selected pixels were then pooled using an empirical cumulative distribution function (ECDF) of their $^{207}Pb/^{235}U$ ratios (termed 'pseudo-analyses' in Drost et al., 2018), with the goal of obtaining the largest possible spread in U-Pb data on a concordia or isochron diagram. The example illustrated in Fig. 7a (modified from Drost et al., 2018; analytical setup detailed in Supplementary Table 1) shows a lacustrine limestone sample consisting of micrite, encrusted bioclasts and calcite spar. The calcite spar crystallized in the interstices of the uncompacted bioclasts and therefore most likely formed during earliest diagenesis. Selecting only pixels with Rb < 0.3 ppm, Zr < 0.3 ppm and Th < 0.3 ppm results in rejection of all pixels corresponding to the bioclast and micrite portions of the sample. These selected pixels (980 of 4203) reflecting the transparent spar were then pooled into 22 analyses, each of which includes c. 30s of signal (45 pixels or timeslices). The lower intercept age of the Tera-Wasserburg regression (300.8 ± 3.7 Ma) was interpreted to be a close estimate of the

depositional age of the lacustrine limestone and the initial $^{207}Pb/^{206}Pb$ ratio (0.858 ± 0.003) is similar to the Stacey and Kramers (1975) terrestrial model Pb at the time. Both intercepts are well constrained which is facilitated by the relatively high U concentration (0.4 to 40 ppm) and the Palaeozoic age of the sample. The bioclasts and micritic calcite turned out to be unsuitable for U-Pb dating because none of the requirements (closed U-Pb system, homogeneous initial Pb isotopic composition and large range in μ) appears to be fulfilled.

The second example (Fig. 7b, modified from Roberts et al., 2020) is from vein calcite with considerably lower U concentrations (< 100 ppb). Macroscopically visible orange alteration is also evident in element maps (high Ba, Sr and Pb) while small veinlets with elevated Cu, Rb, Ba and Pb are also visible (Fig. 7b, left panels). The set of selection criteria was complex in order to (i) select only pixels that belong to the least altered calcite (Ba < 10 ppm, Rb < 0.01 ppm, Cu < 0.2 ppm and ^{238}U < 10,000 counts per second [cps]) and to (ii) clear the data set from spurious data below or around the detection limit (^{206}Pb > 0 cps, ^{207}Pb > 0 cps, ^{208}Pb > 0 cps, ^{238}U > 500 cps, $^{207}Pb/^{206}Pb$ < 1.5, $^{207}Pb/^{206}Pb$ > 0.15, $^{206}Pb/^{208}Pb$ < 10 and $^{206}Pb/^{208}Pb$ > 0.1) because of the low U and Pb concentrations. Pooling the selected pixels (1692 of 4153 pixels) into 29 pseudo-analyses (c. 60s of signal each) gives a lower intercept age of 283.1 ± 9.4 Ma for the least altered calcite within the vein system. This age is similar within uncertainty to the age obtained independently from the same sample by spot analysis using a LA-SF-ICP-MS setup (Roberts et al., 2020).

5. Discussion and future outlook

The advent of LA-ICP-MS mapping in the geosciences presents several challenges in data reduction compared to conventional spot ablation analysis. In conventional spot ablation analysis, signals are usually normalized relative to a reference material (typically a silicate glass or a pressed powder pellet) using an isotope of a major element of invariable concentration across the sample as an internal standard (e.g. a stoichiometric element such as Ca in apatite or Zr in zircon). When the internal standard element does not exhibit constant concentration across the sample (e.g. due to elemental zoning or the sample is comprised of multiple mineral phases with differing concentrations of the internal standard), individual analyses can be normalised using independent constraints on the concentration of the internal standard element (e.g. EPMA or SEM-EDS spot analyses). Internal standard normalization across an entire map is rarely undertaken in LA-ICP-MS mapping as the presence of inclusion or matrix phases within or adjacent to the target phase can result in highly erroneous concentration maps (e.g. consider an apatite inclusion with ppm-level Zr in a zircon with 49.7 wt% Zr), while obtaining EPMA analyses for an internal standard element over the entire mapped area is clearly impractical. Instead LA-ICP-MS mapping experiments usually normalise the time-resolved signal intensities of each element with those of the reference material (a more qualitative form of standardization, termed 'semi-quantified' normalization in Iolite). However, such an approach does not account for matrix-effects (such as differing ablation yields) between the sample and reference material, and the resultant concentration map may not be accurate (e.g. Paul et al., 2014). For a sample comprised primarily of a single mineral phase, 'semi-quantified' normalization of the map followed by application of a simple fractionation factor (determined either from a stoichiometric element or from a region on the map for which there are EPMA or SEM-EDS spot analyses) can be applied to correct for the ablation yield of the main mineral phase. This approach was used for multi-phase LA-ICP-MS mapping experiments undertaken by Paul et al. (2014), who segmented a compositional image of a gabbro sample into different 'phases' and then assigned appropriate internal standard and reference material information to each phase on a pixel-by-pixel basis. Another internal standard-independent calibration strategy was developed by Hoffmann et al. (1997) and utilizes the ion intensities of the major elements to

compensate for different ablation efficiencies. Similarly, Liu et al. (2008) apply a normalization based on the sum of all metal oxides to 100 wt% to obtain a matrix-dependent ablation yield correction factor (AYCF) for semi-quantitative data. This approach is probably the most accurate for most anhydrous minerals and glasses but requires precise knowledge of all participating phases and inclusion of all corresponding major and minor elements in the analyte menu. The strategy will not be successful in the presence of significant anion concentrations such as S, F or Cl but can be modified for e.g. carbonates by normalizing to 100 wt % metal CO_3.

Determinations of uncertainties and limits of detection can also be more challenging in LA-ICP-MS mapping experiments. Uncertainties depend on many factors including (i) elemental concentration, (ii) the presence and nature of interferences on the selected mass, (iii) matrix effects and (iv) accuracy and precision of the reference values of the calibration standard(s). Reporting of uncertainties of individual measurements is not common in routine element concentration determinations derived from LA-ICP-MS maps but is necessary in geochronological applications. While internal uncertainties on a group of pixels (extracted using either manually drawn regions of interest or criteria-based pooling of values) are easy to determine, propagation of uncertainties is more complex. The uncertainty propagation protocol proposed by Horstwood et al. (2016) for LA-ICP-MS U-Pb spot and linear raster analyses can be adapted for image-based U-Pb geochronology (Drost et al., 2018; Roberts et al., 2020). If the internal uncertainties on the reference material have an MSWD greater than 1, an "excess uncertainty" for each analytical session (that accounts for all unquantified sources of analytical uncertainty) should be combined in quadrature with the internal precision derived from each group of pooled pixels to obtain a session-wide uncertainty estimate (*cf* Paton et al., 2010). For comparability with age data acquired in different sessions, in different labs or utilizing different isotope systems, additional systematic uncertainties have to be propagated on the final date by quadratic addition. These include the uncertainty on the age of the reference material, the decay constant uncertainty and a lab- and method-specific long-term reproducibility derived from analyses of a quality control material.

Imaging by LA-ICP-MS presents its own unique challenges to LOD determinations. A detailed treatment is beyond the scope of this review and the reader is advised to consult Petrus et al. (2017), who describe the strengths and limitations of the two main approaches to LOD determinations in LA-ICP-MS analysis (Longerich et al., 1996; Pettke et al., 2012) applied to LA-ICP-MS mapping. Petrus et al. (2017) recommend that as a compromise between low LOD and reasonable time spent measuring backgrounds is to have the number of time slices in the background measurement (N_b) approximately equal to the number of mapped pixels (N_a). They also highlight the problem of analytes with zero background, for which the Longerich et al. (1996) equation produces unrealistic LODs of 0. The Pettke LOD equation is formulated using Poission statistics to accommodate the very low background count rates (c. 1 cps for most of the high mass end of the periodic table) obtained in modern LA-ICP-MS instruments. The LOD and LOQ equations of Howell et al. (2013) were also formulated using a Poisson distribution, and are increasingly being adopted for LA-ICP-MS measurements of elements at the ultra-trace level with very low background count rates . This still leaves the issue of how to represent low concentration LA-ICP-MS data on maps, such as the LREE in olivine which are present at the ppb level (Stead et al., 2017). When part of a multi-element analyte list with short dwell times, many individual pixels will correspond to zero counts. With a non-zero (i.e. 1 cps) background, these pixels are below the LOD and yield negative baseline-corrected counts and concentration data.

The ability to extract and interrogate individual pixels on LA-ICP-MS maps is exceedingly powerful, as it enables evaluation of relationships between elements and / or isotopic ratios at a much higher spatial resolution than conventional spot ablation analysis. Such an approach

has been used to investigate the complexities of gold mineralizing events by identifying fine-scale elemental correlations within sulphides which can then be further explored by geostatistical tools such as multidimensional scaling and discriminant analysis (Gourcerol et al., 2018b), and to investigate the relationship between Th/U ratio and U-Th-Pb age in zircon which demonstrate Th loss along micro-fractures during melt generation (Chew et al., 2017). In both these studies, the data were treated (bilinear interpolation between adjacent traverses and 3×3 pixel smoothing, Gourcerol et al., 2018b; sampling of $4 \times 4\mu m$ "data" blocks from the U-Pb zircon map, Chew et al., 2017) to reduce the effects of sampling a highly transient laser-ablation signal on a sequential mass analyser such as a Q-ICP-MS.

5.1. LA-ICP-based imaging employing simultaneous elemental detection

The advances in low-dispersion laser ablation cells with dispersion times as fast as a few milliseconds (section 3.1; Gundlach-Graham and Günther, 2016) create significant opportunities for the field of LA-ICP-MS imaging. However, as highlighted in section 3.2, low dispersion cells present several challenges for imaging using sequential mass analysers such as those employed in ICP-MS systems, including imaging artefacts (spectral skew) produced by sequential sampling of a transient (pulsed) laser signal (Van Malderen et al., 2018). Simultaneous detection of the entire elemental mass spectrum for each laser shot can account for correlated temporal variations in isotope intensity such as the transient, pulsed nature of laser ablation signals and ICP-MS multiplicative source noise (flicker). Two such approaches are commercially available: double-focusing sector field ICP-MS based on a Mattauch-Herzog geometry and ICP Time-of-flight (TOF) mass analysers. The special characteristic of the Mattauch-Herzog geometry is that all ion masses are focused on one focal plane, which in turn enables the use of a flat surface detector such as a complementary metal oxide semiconductor (CMOS) array. As such it is the only LA-ICP-based system capable of truly simultaneous detection of the entire elemental mass spectrum as a permanent ion beam travels to the detector. While the approach has yet to be widely adopted, future advances in CMOS detection technology might be able to overcome the current limitations in dynamic range associated with TOF mass analysers.

The front end of an ICP-TOF is based on the ICP, ion optics and vacuum of a conventional Q-ICP-MS. The primary ion beam from the ICP is accelerated inside the TOF extraction zone before passing into the field-free flight drift region. The ions gain equal energy from this acceleration and travel at different speeds according to their *m/z* ratio. At the detector, the intensity and time-of-flight of ions from the entire mass spectrum are recorded, yielding a complete mass spectrum for each ion packet. Although the first ICP-TOF instrument was developed in 1994 (Myers et al., 1994), early ICP-TOF instruments suffered from detector non-linearity and yielded significantly lower sensitivities compared to sequential ICP-MS instruments (Burger et al., 2017). In addition, the data acquisition electronics of early generation ICP-TOFs limited the time resolution to substantially below that of the theoretical limits of the TOF mass analyser.

Sensitivity remains a fundamental limitation of ICP-TOF analysis as the TOF analyser can only accept an input pulse of ions after the previous ion packet has been analysed. This ion-throughput limit associated with the duty-factor of TOF-MS results in high-mass end sensitivities that are an order of magnitude lower than a Q-ICP-MS, while the abundance sensitivity of a TOF is approximately three orders of magnitude inferior to that of a Q-ICP-MS at the high mass end (Burger et al., 2017). A Q-ICP-MS also offers three orders of magnitude superior linear dynamic range and superior limits of detection (Hendriks et al., 2017). However, unlike a TOF-MS, a Q-ICP-MS does not conserve its effective sensitivity or LODs based on counting statistics when elements are added to the analyte menu, and a TOF-MS can yield superior effective sensitivity, LODs and signal-to-noise ratios for large elemental menus. Modern TOF-MS instruments such as the icpTOF (TOFWERK AG) can

record the entire element spectrum at 1 kHz and a subset of c. 1000 mass spectra at the full TOF extraction frequency of 33 kHz (Bussweiler et al., 2017; Hendriks et al., 2017). LA-ICP-TOF is thus ideally suited to rapid multi-element analysis of very fast transient signals (i.e. laser ablation imaging in low-dispersion laser ablation cells), while simultaneous detection of the entire elemental mass spectrum also enables more precise isotopic analysis compared to LA-Q-ICP-MS (Ronzani et al., 2018). Triggered acquisition can be employed to enable real-time, spot-resolved multi-element analysis synchronized with the arrival of the sharp ablation peak of the aerosol plume of a single laser shot to the TOF-MS resulting in artefact-free imaging (Bussweiler et al., 2017). Unlike the continuous-scan (rastering) mode of imaging, each spot resolved analysis represents a "closed experiment" where each multi-element pixel can be easily linked to an individual laser shot with precisely defined coordinates. This is essentially an ultrafast version of the 'grid-of-spots' approach described in section 4.1, but availing of the ultrarapid response provided by modern low dispersion cells and the extremely rapid cycle time of an ICP-TOF.

LA-ICP-TOF imaging has now been employed on a variety of biological and geological materials. Example biological imaging applications include imaging of rat kidney samples perfused with the Pt-based anti-cancer drug cisplatin (Bauer et al., 2019) and 3D imaging of the freshwater crustacean *Ceriodaphnia dubia* which was exposed *in vivo* to elevated Cu, Ni, and Zn concentrations (Van Malderen et al., 2017a). Geological applications include imaging of the Opalinus clay, a candidate host rock for a high-level radioactive waste repository in Switzerland (Burger et al., 2015); multi-phase imaging of a kyanite and staurolite-bearing pelitic schist (Burger et al., 2017; Fig. 8a,b); mapping trace element variations in an ore mineral (sphalerite, ZnS) grain with distinct growth zoning (Bussweiler et al., 2017; Fig. 8c, d); imaging the trace-element growth stratigraphy of augite megacrysts from Roman era-volcanism at Stromboli (Ubide et al., 2019b; Fig. 8e, f) 3D elemental imaging of an iron meteorite (He et al., 2017); assigning mineral phases directly from LA-ICP-TOF maps in a mineralogically and texturally complex cataclastic fault rock (Gundlach-Graham et al., 2018; Fig. 8g, h); and elemental mapping of high-pressure, high-temperature reaction experiments to decipher melt-rock reactions in the lithospheric mantle (Bussweiler et al., 2020; Fig. 8i, j).

In addition to rapid, multi-element artefact-free imaging, LA-ICP-TOF mapping offers other advantages. The large multi-element datasets include the major, minor, and trace elements, and phase identification and mass fraction maps can be undertaken using a 100% mass normalization approach to the sum of element species (e.g. Burger et al., 2015, 2017; Gundlach-Graham et al., 2018; Fig. 8a, b), including phase-specific quantification strategies that take into account the mass of major elements based on their molecular stoichiometries when combined with oxide, carbonate or sulfide (e.g. Fig. 8g, h). Such an approach could remove the need for prior SEM-EDS mapping and the associated difficulties in spatial registration and data extraction for multiple images acquired using different microbeam techniques. LA-ICP-MS imaging studies do not conserve effective elemental sensitivities and LODs as the number of elements in the analyte menu is increased, with the result that LA-ICP-MS imaging studies tend to focus on a restricted subset of elements that yield key petrogenetic information. Once LA-ICP-TOF imaging becomes more widespread and routine, the availability of large image datasets containing multiple elements (> 60 is routinely achievable) will facilitate 'mining' multi-element images for hitherto unexplored textural relationships of minor and trace elements in igneous, metamorphic, diagenetic and ore petrogenesis studies.

6. Conclusions

Advances in both LA systems and ICP-MS instruments now permit precise isotopic analysis with laser spot sizes of < 10 μm and sub-ppm detection limits several orders of magnitude superior to SEM-WDS and

SEM-EDS instruments for similar exposure times. Although the spatial resolution and detection limits of LA-Q-ICP-MS systems are inferior to SIMS, the technique is significantly faster, more routinely available, can permit analysis of non-vacuum compatible samples (e.g. living tissues or large archaeological objects that do not fit in the LA cell) and facilitates mapping of large numbers of elements across nearly the entire mass range of the periodic table. Recent innovations in LA and ICP-MS systems include low-dispersion LA cells and dedicated data reduction and image processing packages for visualization, interrogation and extracting quantitative data from maps. These developments have resulted in LA-ICP-MS imaging becoming an important analytical tool in the geosciences, providing high-resolution geochemical information to constrain igneous, metamorphic, ore-forming, sedimentary and diagenetic processes along with their absolute timing.

Magma histories, eruption triggers and ascent rates can be deciphered by LA-ICP-MS mapping of trace-element zonation in (sub-)volcanic macrocrysts. Trace elements in metamorphic rocks are more sensitive than major elements to reactions involving growth and breakdown of accessory minerals and are less prone to diffusive resetting; the large P-T stability field and frequently observed trace-element zonation of garnet make it ideally suited for LA-ICP-MS trace-element mapping. Similarly, the ubiquity of pyrite in ore-bearing and ore-barren systems and its incorporation of a variety of trace elements means it is extensively used in LA-ICP-MS imaging studies applied to ore exploration and petrogenesis. The technique has yet to be extensively applied to clastic or chemical sedimentary rocks, but has great potential for unravelling, characterising and correlating cement growth histories. LA-ICP-MS imaging has also been extensively used in biological and environmental sciences to study catalytic activity in fundamental biological processes; to investigate mobilization mechanisms of low-solubility metals from soil, translocation within plants and their bioavailability; to study disrupted metal homeostasis in age-related neurological disorders and evaluating the distribution and therapeutic impact of metallopharmaceutics in organs.

Imaging is also increasingly used in U-Pb geochronology where many *in situ* geochronological approaches have traditionally employed initial compositional and textural characterization (SEM-EDS or -WDS mapping or CL imaging) of the target phase prior to U-Pb dating by microbeam technique(s). LA-Q-ICP-MS mapping now permits simultaneous acquisition of all the required compositional and U-Pb age information at high-spatial resolution (approaching that of SEM-WDS), while laser ablation split streaming of multi-collector and single collector signals shows great promise for obtaining simultaneous high-precision U-Pb isotopic ratios and trace element data. The approach is ideally suited for U-(Th)-Pb dating of complex polyphase zircon, titanite or monazite where discrete age domains are often linked with specific rock-forming processes and their physical conditions (i.e. U-Pb petrochronology of accessory minerals), along with constraining fine-scale processes affecting the U-Pb zircon systematics when combined with other textural (e.g. CL or Raman) imaging approaches. U-Pb age imaging is particularly suited to geochronology of carbonate minerals which is challenging due to very low U concentrations and appreciable common Pb. The approach facilitates detection of portions of sample which exhibit sufficient spread in $^{238}U/^{204}Pb$ ratio (μ) and simultaneous imaging of trace elements diagnostic of primary carbonate to exclude zones of potential alteration or detrital contamination.

Declaration of Competing Interest

The authors declare that they have no known competing financial interests or personal relationships that could have appeared to influence the work reported in this paper.
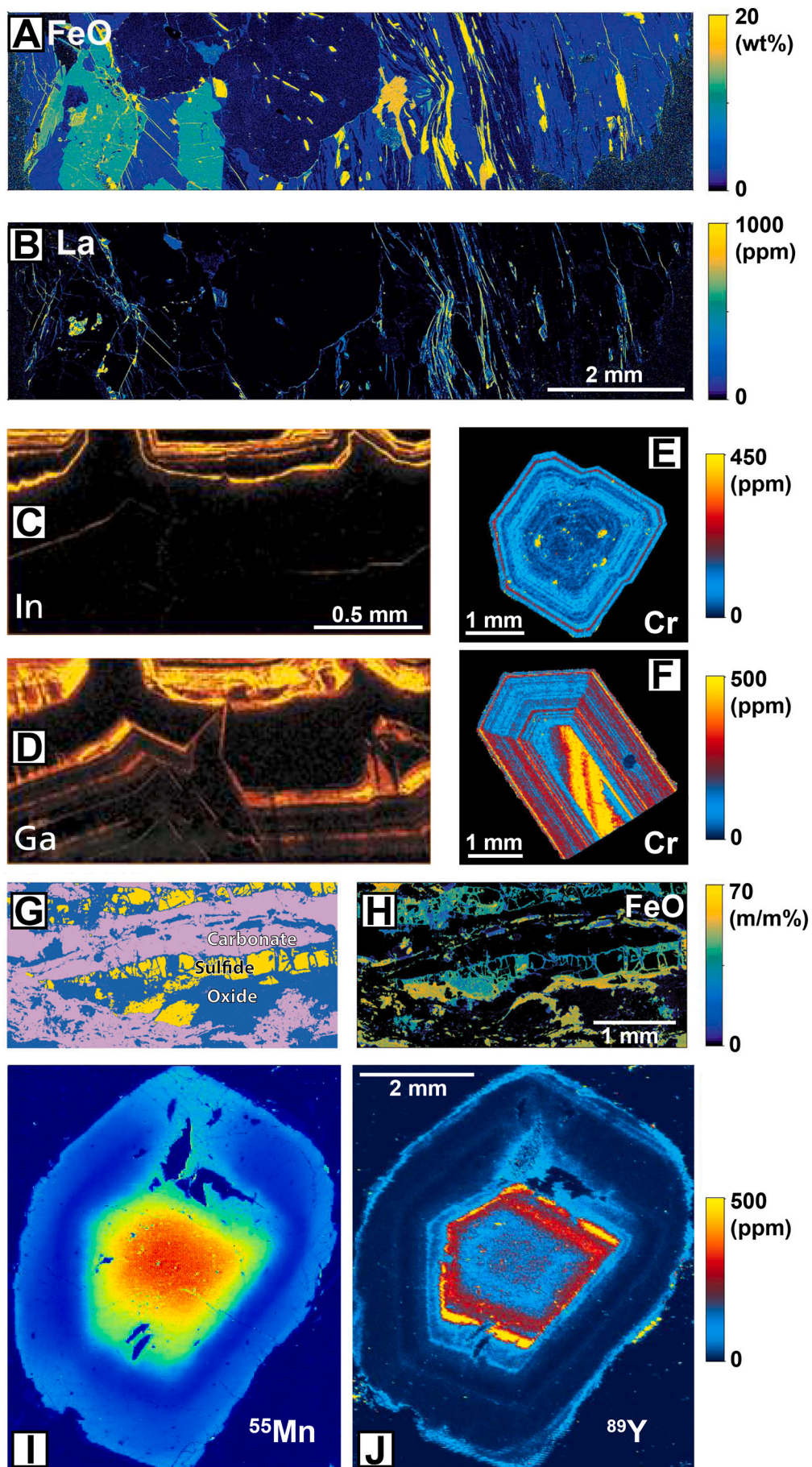
Fig. 8. (ToF Images) A, B) FeO and La maps of a kyanite and staurolite-bearing pelitic schist, modified from Burger et al. (2017); C, D) In and Ga growth zoning in sphalerite (ZnS), modified from Bussweiler et al. (2017); E, F) Cr growth stratigraphy of augite megacrysts cut perpendicular and parallel to the c-axis from a historic eruption at Stromboli, modified from Ubide et al. (2019b); G, H) Fault rock sample (cataclasite) with masks for the carbonate, oxide and sulfide phases generated using 100% normalisation to the sum of element species (panel G), and a quantified image of one of the iron species (FeO – panel H), modified after Gundlach-Graham et al. (2018); I, J) Mn and Y zoning in metamorphic garnet modified after Bussweiler (2017).

Acknowledgements

Appendix A. Supplementary data

Supplementary data to this article can be found online at https://doi.org/10.1016/j.chemgeo.2020.119917.

References

Agangi, A., Hofmann, A., Rollion-Bard, C., Marin-Carbonne, J., Cavalazzi, B., Large, R., Meffre, S., 2015. Gold accumulation in the Archaean Witwatersrand basin, South Africa - evidence from concentrically laminated pyrite. Earth-Science Rev. https://doi.org/10.1016/j.earscirev.2014.10.009.

Arboit, F., Chew, D., Visoná, D., Massironi, M., Sciascia, F., Benedetti, G., Rodani, S., 2019. The geodynamic evolution of the Italian South Alpine basement from the Ediacaran to the Carboniferous: Was the South Alpine terrane part of the peri-Gondwana arc-forming terranes? Gondwana Res. 65, 17–30. https://doi.org/10.1016/j.gr.2018.08.005.

Astbury, R.L., Petrelli, M., Ubide, T., Stock, M.J., Arienzo, I., D'Antonio, M., Perugini, D., 2018. Tracking plumbing system dynamics at the Campi Flegrei caldera, Italy: High-resolution trace element mapping of the Astroni crystal cargo. Lithos 318–319, 464–477. https://doi.org/10.1016/j.lithos.2018.08.033.

Austin, C., Smith, T.M., Bradman, A., Hinde, K., Joannes-Boyau, R., Bishop, D., Hare, D.J., Doble, P., Eskenazi, B., Arora, M., 2013. Barium distributions in teeth reveal early-life dietary transitions in primates. Nature 498, 216–219. https://doi.org/10.1038/nature12169.

Bauer, O.B., Hachmöller, O., Borovinskaya, O., Sperling, M., Schurek, H.J., Ciarimboli, G., Karst, U., 2019. LA-ICP-TOF-MS for rapid, all-elemental and quantitative bioimaging, isotopic analysis and the investigation of plasma processes. J. Anal. At. Spectrom. 34, 694–701. https://doi.org/10.1039/c8ja00288f.

Bellucci, J.J., Nemchin, A.A., Whitehouse, M.J., Kielman, R.B., Snape, J.F., Pidgeon, R.T., 2018. Geochronology of Hadean zircon grains from the Jack Hills, Western Australia constrained by quantitative scanning ion imaging. Chem. Geol. 476, 469–480. https://doi.org/10.1016/j.chemgeo.2017.11.042.

Beyssac, O., Goffé, B., Chopin, C., Rouzaud, J.N., 2002. Raman spectra of carbonaceous material in metasediments: A new geothermometer. J. Metamorph. Geol. 20, 859–871. https://doi.org/10.1046/j.1525-1314.2002.00408.x.

Bonnetti, C., Zhou, L., Riegler, T., Brugger, J., Fairclough, M., 2020. Large S isotope and trace element fractionations in pyrite of uranium roll front systems result from internally-driven biogeochemical cycle. Geochim. Cosmochim. Acta 282, 113–132. https://doi.org/10.1016/j.gca.2020.05.019.

Brenan, J.M., Shaw, H.F., Phinney, D.L., Ryerson, F.J., 1994. Rutile-aqueous fluid partitioning of Nb, Ta, Hf, Zr, U and Th: implications for high field strength element depletions in island-arc basalts. Earth Planet. Sci. Lett. 128, 327–339. https://doi.org/10.1016/0012-821X(94)90154-6.

Burger, M., Gundlach-Graham, A., Allner, S., Schwarz, G., Wang, H.A.O., Gyr, L., Burgener, S., Hattendorf, B., Grolimund, D., Günther, D., 2015. High-Speed, High-Resolution, Multielemental LA-ICP-TOFMS Imaging: Part II. Critical Evaluation of Quantitative Three-Dimensional Imaging of Major, Minor, and Trace Elements in Geological Samples. Anal. Chem. 87, 8259–8267. https://doi.org/10.1021/acs.analchem.5b01977.

Burger, M., Schwarz, G., Gundlach-Graham, A., Käser, D., Hattendorf, B., Günther, D., 2017. Capabilities of laser ablation inductively coupled plasma time-of-flight mass spectrometry. J. Anal. At. Spectrom. 32, 1946–1959. https://doi.org/10.1039/c7ja00236j.

Bussweiler, Y., 2017. Capabilities of the icpTOF for Laser Ablation Applications [WWW Document]. Tofw. AG webinar, URL. https://www.tofwerk.com/wp-content/uploads/2017/09/icpTOF-Webinar-Laser-Ablation-2017.pdf (accessed 4.16.20).

Bussweiler, Y., Foley, S.F., Prelević, D., Jacob, D.E., 2015. The olivine macrocryst problem: New insights from minor and trace element compositions of olivine from Lac de Gras kimberlites, Canada. Lithos 220–223, 238–252. https://doi.org/10.1016/j.lithos.2015.02.016.

Bussweiler, Y., Borovinskaya, O., Tanner, M., 2017. Laser Ablation and inductively coupled plasma-time-of-flight mass spectrometry - A powerful combination for high-speed multielemental imaging on the micrometer scale. Spectroscopy 32, 14–20.

Bussweiler, Y., Gervasoni, F., Rittner, M., Berndt, J., Klemme, S., 2020. Trace element mapping of high-pressure, high-temperature experimental samples with laser ablation ICP time-of-flight mass spectrometry – Illuminating melt-rock reactions in the lithospheric mantle. Lithos 352–353, 105282. https://doi.org/10.1016/j.lithos.2019.105282.

Cave, B.J., Barnes, S.J., Pitcairn, I.K., Sack, P.J., Kuikka, H., Johnson, S.C., Duran, C.J., 2019. Multi-stage precipitation and redistribution of gold, and its collection by lead-bismuth and lead immiscible liquids in a reduced-intrusion related gold system (RIRGS); Dublin Gulch, western Canada. Ore Geol. Rev. 106, 28–55. https://doi.org/10.1016/j.oregeorev.2019.01.010.

Cesar da Silva, J., Pacureanu, A., Yang, Y., Bohic, S., Morawe, C., Barrett, R., Cloetens, P., 2017. Efficient concentration of high-energy x-rays for diffraction-limited imaging resolution. Optica 4, 492. https://doi.org/10.1364/optica.4.000492.

Chen, Y., Zou, C., Mastalerz, M., Hu, S., Gasaway, C., Tao, X., 2015. Applications of micro-fourier transform infrared spectroscopy (FTIR) in the geological sciences—A Review. Int. J. Mol. Sci. https://doi.org/10.3390/ijms161226227.

Chew, D.M., Schaltegger, U., Košler, J., Whitehouse, M.J., Gutjahr, M., Spikings, R.A., Mišković, A., 2007. U-Pb geochronologic evidence for the evolution of the Gondwanan margin of the north-central Andes. Bull. Geol. Soc. Am. 119, 697–711. https://doi.org/10.1130/B26080.1.

Chew, D.M., Petrus, J.A., Kenny, G.G., McEvoy, N., 2017. Rapid high-resolution U-Pb LA-Q-ICPMS age mapping of zircon. J. Anal. At. Spectrom. 32, 262–276. https://doi.org/10.1039/c6ja00404k.

Chew, D., Drost, K., Petrus, J.A., 2019. Ultrafast, > 50 Hz LA-ICP-MS Spot Analysis Applied to U–Pb Dating of Zircon and other U-Bearing Minerals. Geostand. Geoanalytical Res. 43, 39–60. https://doi.org/10.1111/ggr.12257.

Conn, C.D., Spry, P.G., Layton-Matthews, D., Voinot, A., Koenig, A., 2019. The effects of amphibolite facies metamorphism on the trace element composition of pyrite and pyrrhotite in the Cambrian Nairne Pyrite Member, Kanmantoo Group. South Australia. Ore Geol. Rev. 114. https://doi.org/10.1016/j.oregeorev.2019.103128.

Cook, N.J., Ciobanu, C.L., Meria, D., Silcock, D., Wade, B., 2013. Arsenopyrite-pyrite association in an orogenic gold ore: Tracing mineralization history from textures and trace elements. Econ. Geol. 108, 1273–1283. https://doi.org/10.2113/econgeo.108.6.1273.

Corrie, S.L., Kohn, M.J., 2008. Trace-element distributions in silicates during prograde metamorphic reactions: Implications for monazite formation. J. Metamorph. Geol. 26, 451–464. https://doi.org/10.1111/j.1525-1314.2008.00769.x.

Courtney-Davies, L., Ciobanu, C.L., Verdugo-Ihl, M.R., Dmitrijeva, M., Cook, N.J., Ehrig, K., Wade, B.P., 2019. Hematite geochemistry and geochronology resolve genetic and temporal links among iron-oxide copper gold systems, Olympic Dam district, South Australia. Precambrian Res. 335. https://doi.org/10.1016/j.precamres.2019.105480.

Craig, G., Horstwood, M.S.A., Reid, H.J., Sharp, B.L., 2020. 'Blind time'-current limitations on laser ablation multi-collector inductively coupled plasma mass spectrometry (LA-MC-ICP-MS) for ultra-transient signal isotope ratio analysis and application to individual sub-micron sized uranium particles. J. Anal. At. Spectrom. 35, 1011–1021. https://doi.org/10.1039/d0ja00066c.

Dare, S.A.S., Barnes, S.J., Beaudoin, G., Méric, J., Boutroy, E., Potvin-Doucet, C., 2014. Trace elements in magnetite as petrogenetic indicators. Miner. Depos. 49, 785–796. https://doi.org/10.1007/s00126-014-0529-0.

Dare, S.A.S., Barnes, S.J., Beaudoin, G., 2015. Did the massive magnetite "lava flows" of El Laco (Chile) form by magmatic or hydrothermal processes? New constraints from magnetite composition by LA-ICP-MS. Miner. Depos. 50, 607–617. https://doi.org/10.1007/s00126-014-0560-1.

Della Ventura, G., Bellatreccia, F., Marcelli, A., Cestelli Guidi, M., Piccinini, M., Cavallo, A., Piochi, M., 2010. Application of micro-FTIR imaging in the Earth sciences. Anal. Bioanal. Chem. https://doi.org/10.1007/s00216-010-3811-8.

Depiné, M., Frimmel, H.E., Emsbo, P., Koenig, A.E., Kern, M., 2013. Trace element distribution in uraninite from Mesoarchaean Witwatersrand conglomerates (South Africa) supports placer model and magmatogenic source. Miner. Depos. https://doi.org/10.1007/s00126-013-0458-3.

Draxler, J., Zitek, A., Meischel, M., Stranzl-Tschegg, S.E., Mingler, B., Martinelli, E., Weinberg, A.M., Prohaska, T., 2015. Regionalized quantitative LA-ICP-MS imaging of the biodegradation of magnesium alloys in bone tissue. J. Anal. At. Spectrom. 30, 2459–2468. https://doi.org/10.1039/c5ja00354g.

Drost, K., Chew, D., Petrus, J.A., Scholze, F., Woodhead, J.D., Schneider, J.W., Harper, D.A.T., 2018. An Image Mapping Approach to U-Pb LA-ICP-MS Carbonate Dating and Applications to Direct Dating of Carbonate Sedimentation. Geochemistry, Geophys. Geosystems 19, 4631–4648. https://doi.org/10.1029/2018GC007850.

Eggins, S.M., Shelley, J.M.G., 2002. Compositional Heterogeneity in NIST SRM 610-617 Glasses. Geostand. Geoanalytical Res. 26, 269–286. https://doi.org/10.1111/j.1751-908x.2002.tb00634.x.

Eggins, S., Grün, R., Pike, A.W.G., Shelley, M., Taylor, L., 2003. 238U, 232Th profiling and U-series isotope analysis of fossil teeth by laser ablation-ICPMS, in: Quaternary Science Reviews. pp. 1373–1382. https://doi.org/10.1016/S0277-3791(03)00064-7.

Eggins, S.M., Grün, R., McCulloch, M.T., Pike, A.W.G., Chappell, J., Kinsley, L., Mortimer, G., Shelley, M., Murray-Wallace, C.V., Spötl, C., Taylor, L., 2005. In situ U-series dating by laser-ablation multi-collector ICPMS: New prospects for Quaternary geochronology. Quat. Sci. Rev. 24, 2523–2538. https://doi.org/10.1016/j.quascirev.2005.07.006.

El Korh, A., Schmidt, S.T., Ulianov, A., Potel, S., 2009. Trace element partitioning in HP-LT metamorphic assemblages during subduction-related metamorphism, Ile de Groix, France: A detailed LA-ICPMS study. J. Petrol. 50, 1107–1148. https://doi.org/10.1093/petrology/egp034.

Emsbo, P., McLaughlin, P.I., Breit, G.N., du Bray, E.A., Koenig, A.E., 2015. Rare earth elements in sedimentary phosphate deposits: Solution to the global REE crisis? Gondwana Res. https://doi.org/10.1016/j.gr.2014.10.008.

Engi, M., 2017. Petrochronology Based on REE-Minerals: Monazite, Allanite, Xenotime, Apatite, in: Kohn, M.J., Engi, M., Lanari, P. (Eds.), Petrochronology: Methods and Applications. Reviews in Mineralogy and Geochemistry 83 (1), 365–418. https://doi.org/10.2138/rmg.2017.83.12.

Engi, M., Lanari, P., Kohn, M.J., 2017. Significant Ages-An Introduction to Petrochronology, in: Kohn, M.J., Engi, M., Lanari, P. (Eds.), Petrochronology: Methods and Applications. Reviews in Mineralogy and Geochemistry 83 (1), 1–12. https://doi.org/10.2138/rmg.2017.83.1.

Evans, D., Müller, W., 2013. LA-ICPMS elemental imaging of complex discontinuous carbonates: An example using large benthic foraminifera. J. Anal. At. Spectrom. 28, 1039–1044. https://doi.org/10.1039/c3ja50053e.

Fabre, C., Devismes, D., Moncayo, S., Pelascini, F., Trichard, F., Lecomte, A., Bousquet, B., Cauzid, J., Motto-Ros, V., 2018. Elemental imaging by laser-induced breakdown spectroscopy for the geological characterization of minerals. J. Anal. At. Spectrom. 33, 1345–1353. https://doi.org/10.1039/c8ja00048d.

Fernández, B., 2019. Elemental and molecular imaging by LA-ICP-MS. Anal. Bioanal. Chem. 411, 547–548. https://doi.org/10.1007/s00216-018-1523-7.

Fietzke, J., Ragazzola, F., Halfar, J., Dietze, H., Foster, L.C., Hansteen, T.H., Eisenhauer, A., Steneck, R.S., 2015. Century-scale trends and seasonality in pH and temperature for shallow zones of the Bering Sea. Proc. Natl. Acad. Sci. U. S. A. 112, 2960–2965. https://doi.org/10.1073/pnas.1419216112.

Fox, M., Tripathy-Lang, A., Shuster, D.L., 2017. Improved spatial resolution of elemental maps through inversion of LA-ICP-MS data. Chem. Geol. 467, 30–41. https://doi.org/10.1016/j.chemgeo.2017.07.001.

Gallagher, M., Turner, E.C., Kamber, B.S., 2015. In situ trace metal analysis of Neoarchean - Ordovician shallow-marine microbial-carbonate-hosted pyrites. Geobiology 13, 316–339. https://doi.org/10.1111/gbi.12139.

Gehrels, G.E., Valencia, V.A., Ruiz, J., 2008. Enhanced precision, accuracy, efficiency, and spatial resolution of U-Pb ages by laser ablation-multicollector-inductively coupled plasma-mass spectrometry. Geochemistry, Geophys. Geosystems 9. https://doi.org/10.1029/2007GC001805.

Genna, D., Gaboury, D., 2015. Deciphering the hydrothermal evolution of a VMS System by LA-ICP-MS using trace elements in pyrite: An example from the Bracemac-McLeod deposits, Abitibi, Canada, and implications for exploration. Econ. Geol. 110, 2087–2108. https://doi.org/10.2113/econgeo.110.8.2087.

George, L., Cook, N.J., Cristiana, C., Wade, B.P., 2015. Trace and minor elements in galena: A reconnaissance LA-ICP-MS study. Am. Mineral. 100, 548–569. https://doi.org/10.2138/am-2015-4862.

George, F.R., Gaidies, F., Boucher, B., 2018. Population-wide garnet growth zoning revealed by LA-ICP-MS mapping: implications for trace element equilibration and syn-kinematic deformation during crystallisation. Contrib. to Mineral. Petrol. 173. https://doi.org/10.1007/s00410-018-1503-0.

Gourcerol, B., Kontak, D.J., Thurston, P.C., Petrus, J.A., 2018a. Results of LA-ICP-MS sulfide mapping from Algoma-type BIF gold systems with implications for the nature of mineralizing fluids, metal sources, and deposit models. Miner. Depos. 53, 871–894. https://doi.org/10.1007/s00126-017-0788-7.

Gourcerol, B., Kontak, D.J., Thurston, P.C., Petrus, J.A., 2018b. Application of LA-ICP-MS sulfide analysis and methodology for deciphering elemental paragenesis and associations in addition to multi-stage processes in metamorphic gold settings. Can. Mineral. 56, 39–64. https://doi.org/10.3749/canmin.1700048.

Gray, A.L., 1985. Solid sample introduction by laser ablation for inductively coupled plasma source mass spectrometry. Analyst 110, 551–556. https://doi.org/10.1039/AN9851000551.

Gu, H.O., Sun, H., Wang, F., Ge, C., Zhou, T., 2019. A new practical isobaric interference correction model for the in situ Hf isotopic analysis using laser ablation-multi-collector-ICP-mass spectrometry of zircons with high Yb/Hf ratios. J. Anal. At. Spectrom. 34, 1223–1232. https://doi.org/10.1039/c9ja00024k.

Guillong, M., Meier, D.L., Allan, M.M., Heinrich, C.A., Yardley, B.W.D., 2008. SILLS: A MATLAB-based program for the reduction of laser ablation ICP–MS data of homogeneous materials and inclusions. In: Sylvester, P.J. (Ed.), Laser Ablation ICP-MS in the Earth Sciences: Current Practices and Outstanding Issues. Mineralogical Association of Canada Short Course. 40. B.C., Vancouver, pp. 328–333.

Gundlach-Graham, A., Günther, D., 2016. Toward faster and higher resolution LA–ICPMS imaging: on the co-evolution of LA cell design and ICPMS instrumentation. Anal. Bioanal. Chem. 408, 2687–2695. https://doi.org/10.1007/s00216-015-9251-8.

Gundlach-Graham, A., Garofalo, P.S., Schwarz, G., Redi, D., Günther, D., 2018. High-resolution, Quantitative Element Imaging of an Upper Crust, Low-angle Cataclasite (Zuccale Fault, Northern Apennines) by Laser Ablation ICP Time-of-Flight Mass Spectrometry. Geostand. Geoanalytical Res. 42, 559–574. https://doi.org/10.1111/ggr.12233.

Günther, D., Hattendorf, B., 2005. Solid sample analysis using laser ablation inductively coupled plasma mass spectrometry. TrAC - Trends Anal. Chem. 24, 255–265. https://doi.org/10.1016/j.trac.2004.11.017.

Stacey, J.S., Kramers, J.D., 1975. Approximation of terrestrial lead isotope evolution by a two-stage model. Earth Planet. Sci. Lett. 26, 207–221. https://doi.org/10.1007/s00216-011-5461-x.

Guo, J., Zhang, R., Li, C., Sun, W., Hu, Y., Kang, D., Wu, J., 2018. Genesis of the Gaosong Sn–Cu deposit, Gejiu district, SW China: Constraints from in situ LA-ICP-MS cassiterite U–Pb dating and trace element fingerprinting. Ore Geol. Rev. 92, 627–642. https://doi.org/10.1016/j.oregeorev.2017.11.033.

Hare, D.J., Kysenius, K., Paul, B., Knauer, B., Hutchinson, R.W., O'Connor, C., Fryer, F., Hennessey, T.P., Bush, A.I., Crouch, P.J., Doble, P.A., 2017. Imaging Metals in Brain Tissue by Laser Ablation - Inductively Coupled Plasma - Mass Spectrometry (LA-ICP-MS). J. Vis. Exp. 119, e55042. https://doi.org/10.3791/55042.

Hattendorf, B., Hartfelder, U., Günther, D., 2019. Skip the beat: minimizing aliasing error in LA-ICP-MS measurements. Anal. Bioanal. Chem. 411, 591–602. https://doi.org/10.1007/s00216-018-1314-1.

He, M., Meng, Y., Yan, S., Hang, W., Zhou, W., Huang, B., 2017. Three-dimensional elemental imaging of Nantan meteorite via femtosecond laser ionization time-of-flight mass spectrometry. Anal. Chem. 89, 565–570. https://doi.org/10.1021/acs.analchem.6b03540.

Hellstrom, J.C., Paton, C., Woodhead, J.D., Hergt, M., 2008. Iolite: Software for spatially resolved LA-(quad and MC) ICP-MS analysis. In: Sylvester, P. (Ed.), Laser Ablation ICP-MS in the Earth Sciences: Current Practices and Outstanding Issues. Mineralogical Association of Canada Short Course. 40. B.C., Vancouver, pp. 343–348.

Hendriks, L., Gundlach-Graham, A., Hattendorf, B., Günther, D., 2017. Characterization of a new ICP-TOFMS instrument with continuous and discrete introduction of solutions. J. Anal. At. Spectrom. 32, 548–561. https://doi.org/10.1039/c6ja00400h.

Henrichs, I.A., O'Sullivan, G., Chew, D.M., Mark, C., Babechuk, M.G., McKenna, C., Emo, R., 2018. The trace element and U-Pb systematics of metamorphic apatite. Chem. Geol. 483, 218–238. https://doi.org/10.1016/j.chemgeo.2017.12.031.

Henrichs, I.A., Chew, D.M., O'Sullivan, G.J., Mark, C., McKenna, C., Guyett, P., 2019. Trace Element (Mn-Sr-Y-Th-REE) and U-Pb Isotope Systematics of Metapelitic Apatite During Progressive Greenschist- to Amphibolite-Facies Barrovian Metamorphism. Geochemistry, Geophys. Geosystems 20, 4103–4129. https://doi.org/10.1029/2019GC008359.

Hetherington, C.J., Backus, E.L., McFarlane, C.R.M., Fisher, C.M., Graham, P.D., 2017. Origins of textural, compositional, and isotopic complexity in monazite and its petrochronological analysis, in: Moser, D.E., Corfu, F., Darling, J.R., Reddy, S.M., Tait, K. (Eds.), Microstructural Geochronology: Planetary Records Down to Atom Scale. pp. 63–90. https://doi.org/10.1002/9781119227250.ch3.

Hnatyshin, D., Creaser, R.A., Meffre, S., Stern, R.A., Wilkinson, J.J., Turner, E.C., 2020. Understanding the microscale spatial distribution and mineralogical residency of Re in pyrite: Examples from carbonate-hosted Zn-Pb ores and implications for pyrite Re-Os geochronology. Chem. Geol. 533. https://doi.org/10.1016/j.chemgeo.2019.119427.

Hoffmann, E., Lüdke, C., Scholze, H., 1997. Is laser-ablation-ICP-MS an alternative to solution analysis of solid samples? Fresenius. J. Anal. Chem. 359, 394–398. https://doi.org/10.1007/s002160050595.

Hopkinson, T.N., Harris, N.B.W., Warren, C.J., Spencer, C.J., Roberts, N.M.W., Horstwood, M.S.A., Parrish, R.R., EIMF, 2017. The identification and significance of pure sediment-derived granites. Earth Planet. Sci. Lett. 467, 57–63. https://doi.org/10.1016/j.epsl.2017.03.018.

Horstwood, M.S.A., Košler, J., Gehrels, G., Jackson, S.E., McLean, N.M., Paton, C., Pearson, N.J., Sircombe, K., Sylvester, P., Vermeesch, P., Bowring, J.F., Condon, D.J., Schoene, B., 2016. Community-derived standards for LA-ICP-MS U-(Th-)Pb geochronology – uncertainty propagation, age interpretation and data reporting. Geostand. Geoanalytical Res. 40, 311–332. https://doi.org/10.1111/j.1751-908X.2016.00379.x.

Horton, F., Hacker, B., Kylander-Clark, A., Holder, R., Jöns, N., 2016. Focused radiogenic heating of middle crust caused ultrahigh temperatures in southern Madagascar. Tectonics 35, 293–314. https://doi.org/10.1002/2015TC004040.

Howell, D., Griffin, W.L., Pearson, N.J., Powell, W., Wieland, P., O'Reilly, S.Y., 2013. Trace element partitioning in mixed-habit diamonds. Chem. Geol. 355, 134–143. https://doi.org/10.1016/j.chemgeo.2013.07.013.

Jahn, Ming, B., Cuvellier, H., 1994. Pb-Pb and U-Pb geochronology of carbonate rocks: an assessment. Chem. Geol. 115, 125–151. https://doi.org/10.1016/0009-2541(94)90149-X.

Jankovics, M.É., Sági, T., Astbury, R.L., Petrelli, M., Kiss, B., Ubide, T., Németh, K., Ntaflos, T., Harangi, S., 2019. Olivine major and trace element compositions coupled with spinel chemistry to unravel the magmatic systems feeding monogenetic basaltic volcanoes. J. Volcanol. Geotherm. Res. 369, 203–223. https://doi.org/10.1016/j.jvolgeores.2018.11.027.

Jochum, K.P., Stoll, B., Herwig, K., Willbold, M., 2007. Validation of LA-ICP-MS trace element analysis of geological glasses using a new solid-state 193 nm Nd : YAG laser and matrix-matched calibration. J. Anal. At. Spectrom. 22, 112–121. https://doi.org/10.1039/b609547j.

Jochum, K.P., Stoll, B., Weis, U., Jacob, D.E., Mertz-Kraus, R., Andreae, M.O., 2014. Non-Matrix-Matched Calibration for the Multi-Element Analysis of Geological and Environmental Samples Using 200 nm Femtosecond LA-ICP-MS: A Comparison with Nanosecond Lasers. Geostand. Geoanalytical Res. 38, 265–292. https://doi.org/10.1111/j.1751-908X.2014.12028.x.

Kaeter, D., Barros, R., Menuge, J.F., Chew, D.M., 2018. The magmatic–hydrothermal transition in rare-element pegmatites from southeast Ireland: LA-ICP-MS chemical mapping of muscovite and columbite–tantalite. Geochim. Cosmochim. Acta 240, 98–130. https://doi.org/10.1016/j.gca.2018.08.024.

Kelly, C.J., Schneider, D.A., Jackson, S.E., Kalbfleisch, T., McFarlane, C.R., 2017. Insights into low- to moderate-temperature recrystallization of zircon: Unpolished crystal depth profile techniques and geochemical mapping. Chem. Geol. 449, 82–98. https://doi.org/10.1016/j.chemgeo.2016.11.035.

Kilburn, M.R., Wacey, D., 2015. Nanoscale secondary ion mass spectrometry (NanoSIMS) as an analytical tool in the geosciences. RSC Detect. Sci. Series 4, 1–34. https://doi.org/10.1039/9781782625025-00001.

Kimura, J.I., Chang, Q., Kanazawa, N., Sasaki, S., Vaglarov, B.S., 2016. High-precision in situ analysis of Pb isotopes in glasses using 10^{13} Ω resistor high gain amplifiers with ultraviolet femtosecond laser ablation multiple Faraday collector inductively coupled plasma mass spectrometry. J. Anal. At. Spectrom. 31, 790–800. https://doi.org/10.1039/c5ja00374a.

Kohn, M.J., 2014. Geochemical Zoning in Metamorphic Minerals. In: Holland, H.D., Turekian, K.K. (Eds.), Treatise on Geochemistry, Second edition. pp. 249–280. https://doi.org/10.1016/B978-0-08-095975-7.00307-7.

Kohn, M.J., 2017. Titanite Petrochronology, in: Kohn, M.J., Engi, M., Lanari, P. (Eds.), Petrochronology: Methods and Applications. Reviews in Mineralogy and Geochemistry 83 (1), 419–441. https://doi.org/10.2138/rmg.2017.83.13.

Košler, J., 2008. Laser ablation sampling strategies for concentration and isotope ratio

analyses by ICP-MS. In: Sylvester, P.J. (Ed.), Laser Ablation–ICP–MS in the Earth Sciences: Current Practices and Outstanding Issues. Mineralogical Association of Canada Short Course. 40. B.C., Vancouver, pp. 79–92.

Kröner, A., Wan, Y., Liu, X., Liu, D., 2014. Dating of zircon from high-grade rocks: Which is the most reliable method? Geosci. Front. 5, 515–523. https://doi.org/10.1016/j.gsf.2014.03.012.

Kuisma-Kursula, P., 2000. Accuracy, Precision and Detection Limits of SEM-WDS, SEM-EDS and PIXE in the Multi-Elemental Analysis of Medieval Glass. X-Ray Spectrom 29, 111–118. https://doi.org/10.1002/(SICI)1097-4539(200001/02)29:1<111::AID-XRS408>3.0.CO;2-W.

Kylander-Clark, A.R.C., Hacker, B.R., Cottle, J.M., 2013. Laser-ablation split-stream ICP petrochronology. Chem. Geol. 345, 99–112. https://doi.org/10.1016/j.chemgeo.2013.02.019.

Lanari, P., Vidal, O., De Andrade, V., Dubacq, B., Lewin, E., Grosch, E.G., Schwartz, S., 2014. XMapTools: A MATLAB©-based program for electron microprobe X-ray image processing and geothermobarometry. Comput. Geosci. 62, 227–240. https://doi.org/10.1016/j.cageo.2013.08.010.

Large, R.R., Danyushevsky, L., Hollit, C., Maslennikov, V., Meffre, S., Gilbert, S., Bull, S., Scott, R., Emsbo, P., Thomas, H., Singh, B., Foster, J., 2009. Gold and trace element zonation in pyrite using a laser imaging technique: Implications for the timing of gold in orogenic and Carlin-style sediment-hosted deposits. Econ. Geol. 104, 635–668. https://doi.org/10.2113/gsecongeo.104.5.635.

Li, X.H., Li, Q.L., 2016. Major advances in microbeam analytical techniques and their applications in Earth Science. Sci. Bull. 61, 1785–1787. https://doi.org/10.1007/s11434-016-1197-5.

Li, D., Fu, Y., Sun, X., Hollings, P., Liao, J., Liu, Q., Feng, Y., Liu, Y., Lai, C., 2018. LA-ICP-MS trace element mapping: Element mobility of hydrothermal magnetite from the giant Beiya Fe-Au skarn deposit. SW China. Ore Geol. Rev. 92, 463–474. https://doi.org/10.1016/j.oregeorev.2017.11.027.

Li, D., Fu, Y., Liu, Q., Reinfelder, J.R., Hollings, P., Sun, X., Tan, C., Dong, Y., Ma, W., 2020. High-resolution LA-ICP-MS mapping of deep-sea polymetallic micronodules and its implications on element mobility. Gondwana Res. 81, 461–474. https://doi.org/10.1016/j.gr.2019.12.009.

Liu, Y., Hu, Z., Gao, S., Günther, D., Xu, J., Gao, C., Chen, H., 2008. In situ analysis of major and trace elements of anhydrous minerals by LA-ICP-MS without applying an internal standard. Chem. Geol. 257, 34–43. https://doi.org/10.1016/j.chemgeo.2008.08.004.

Longerich, H.P., Jackson, S.E., Günther, D., 1996. Laser ablation inductively coupled plasma mass spectrometric transient signal data acquisition and analyte concentration calculation. J. Anal. At. Spectrom. 11, 899–904. https://doi.org/10.1039/JA9961100899.

López-Fernández, H., De, S., Pessôa, G., Arruda, M.A.Z., Capelo-Martínez, J.L., Fdez-Riverola, F., Glez-Peña, D., Reboiro-Jato, M., 2016. LA-iMageS: a software for ele-mental distribution bioimaging using LA-ICP-MS data. J. Cheminform. 8, 1–10. https://doi.org/10.1186/s13321-016-0178-7.

Lünsdorf, Kalies, Ahlers, Dunkl, Eynatten, von, 2019. Semi-Automated Heavy-Mineral Analysis by Raman Spectroscopy. Minerals 9, 385. https://doi.org/10.3390/min9070385.

Lyon, I.C., Kusiak, M.A., Wirth, R., Whitehouse, M.J., Dunkley, D.J., Wilde, S.A., Schaumlöffel, D., Malherbe, J., Moore, K.L., 2019. Pb nanospheres in ancient zircon yield model ages for zircon formation and Pb mobilization. Sci. Rep. 9. https://doi.org/10.1038/s41598-019-49882-8.

Majumda, S., Peralta-Videa, J.R., Castillo-Michel, H., Hong, J., Rico, C.M., Gardea-Torresdey, J.L., 2012. Applications of synchrotron μ-XRF to study the distribution of biologically important elements in different environmental matrices: A review. Anal. Chim. Acta 755, 1–16. https://doi.org/10.1016/j.aca.2012.09.050.

Managh, A.J., Reid, P., 2019. A new freeware tool for image processing and its applica-tion to high speed LA-ICP-MS imaging. J. Anal. At. Spectrom. 34, 1369–1373. https://doi.org/10.1039/c9ja00082h.

Marsh, J.H., Stockli, D.F., 2015. Zircon U-Pb and trace element zoning characteristics in an anatectic granulite domain: Insights from LASS-ICP-MS depth profiling. Lithos 239, 170–185. https://doi.org/10.1016/j.lithos.2015.10.017.

Marsh, J.H., Gerbi, C.C., Culshaw, N.G., Johnson, S.E., Wooden, J.L., Clark, C., 2012. Using zircon U-Pb ages and trace element chemistry to constrain the timing of me-tamorphic events, pegmatite dike emplacement, and shearing in the southern Parry Sound domain, Grenville Province, Canada. Precambrian Res. 192–195, 142–165. https://doi.org/10.1016/j.precamres.2011.10.017.

Mischel, S.A., Mertz-Kraus, R., Jochum, K.P., Scholz, D., 2017. TERMITE: An R script for fast reduction of laser ablation inductively coupled plasma mass spectrometry data and its application to trace element measurements. Rapid Commun. Mass Spectrom. 31, 1079–1087. https://doi.org/10.1002/rcm.7895.

Moreno-Gordaliza, E., Giesen, C., Lázaro, A., Esteban-Fernández, D., Humanes, B., Cañas, B., Panne, U., Tejedor, A., Jakubowski, N., Gómez-Gómez, M.M., 2011. Elemental bioimaging in kidney by LA-ICP-MS as a tool to study nephrotoxicity and renal protective strategies in cisplatin therapies. Anal. Chem. 83, 7933–7940. https://doi.org/10.1021/ac201933x.

Morgan, G.B.VI., London, D., 1996. Optimizing the electron microprobe analysis of hy-drous alkali aluminosilicate glasses. Am. Mineral. 81, 1176–1185. https://doi.org/10.2138/am-1996-9-1016.

Mouchi, V., Crowley, Q.G., Ubide, T., 2016. AERYN: A simple standalone application for visualizing and enhancing elemental maps. Appl. Geochemistry 75, 44–53. https://doi.org/10.1016/j.apgeochem.2016.10.012.

Müller, W., Shelley, M., Miller, P., Broude, S., 2009. Initial performance metrics of a new custom-designed ArF excimer LA-ICPMS system coupled to a two-volume laser-ab-lation cell. J. Anal. At. Spectrom. 24, 209–214. https://doi.org/10.1039/B805995K.

Myers, D.P., Li, G., Yang, P., Hieftje, G.M., 1994. An inductively coupled plasma-time-of-flight mass spectrometer for elemental analysis. Part I: Optimization and character-istics. J. Am. Soc. Mass Spectrom. 5, 1008–1016. https://doi.org/10.1016/1044-0305(94)80019-7.

Nasdala, L., Lengauer, C.L., Hanchar, J.M., Kronz, A., Wirth, R., Blanc, P., Kennedy, A.K., Seydoux-Guillaume, A.M., 2002. Annealing radiation damage and the recovery of cathodoluminescence. Chem. Geol. 191, 121–140. https://doi.org/10.1016/S0009-2541(02)00152-3.

Neumann, B., Hösl, S., Schwab, K., Theuring, F., Jakubowski, N., 2020. Multiplex LA-ICP-MS bio-imaging of brain tissue of a parkinsonian mouse model stained with metal-coded affinity-tagged antibodies and coated with indium-spiked commercial inks as internal standards. J. Neurosci. Methods 334, 108591. https://doi.org/10.1016/j.jneumeth.2020.108591.

Newbury, D.E., Ritchie, N.W.M., 2013. Is scanning electron microscopy/energy dispersive X-ray spectrometry (SEM/EDS) quantitative? Scanning 35, 141–168. https://doi.org/10.1002/sca.21041.

Newbury, D.E., Ritchie, N.W.M., 2015. Performing elemental microanalysis with high accuracy and high precision by scanning electron microscopy/silicon drift detector energy-dispersive X-ray spectrometry (SEM/SDD-EDS). J. Mater. Sci. https://doi.org/10.1007/s10853-014-8685-2.

O'Sullivan, G., Chew, D., Kenny, G., Henrichs, I., Mulligan, D., 2020. The trace element composition of apatite and its application to detrital provenance studies. Earth-Science Rev. 201, 103044. https://doi.org/10.1016/j.earscirev.2019.103044.

Park, C., Choi, W., Kim, H., Park, M.H., Kang, I.M., Lee, H.S., Song, Y., 2017. Oscillatory zoning in skarn garnet: Implications for tungsten ore exploration. Ore Geol. Rev. 89, 1006–1018. https://doi.org/10.1016/j.oregeorev.2017.08.003.

Paton, C., Woodhead, J.D., Hellstrom, J.C., Hergt, J.M., Greig, A., Maas, R., 2010. Improved laser ablation U-Pb zircon geochronology through robust downhole frac-tionation correction. Geochemistry, Geophys. Geosystems 11. https://doi.org/10.1029/2009GC002618.

Paton, C., Hellstrom, J., Paul, B., Woodhead, J., Hergt, J., 2011. Iolite: Freeware for the visualisation and processing of mass spectrometric data. J. Anal. At. Spectrom. 26, 2508–2518. https://doi.org/10.1039/C1ja10172b.

Paul, B., Paton, C., Norris, A., Woodhead, J., Hellstrom, J., Hergt, J., Greig, A., 2012. CellSpace: A module for creating spatially registered laser ablation images within the Iolite freeware environment. J. Anal. At. Spectrom. 27, 700–706. https://doi.org/10.1039/c2ja10383d.

Paul, B., Woodhead, J.D., Paton, C., Hergt, J.M., Hellstrom, J., Norris, C.A., 2014. Towards a method for quantitative LA-ICP-MS imaging of multi-phase assemblages: Mineral identification and analysis correction procedures. Geostand. Geoanalytical Res. 38, 253–263. https://doi.org/10.1111/j.1751-908X.2014.00270.x.

Petrus, J.A., Chew, D.M., Leybourne, M.I., Kamber, B.S., 2017. A new approach to laser-ablation inductively-coupled-plasma mass-spectrometry (LA-ICP-MS) using the flex-ible map interrogation tool 'Monocle.'. Chem. Geol. 463, 76–93. https://doi.org/10.1016/j.chemgeo.2017.04.027.

Pettke, T., Oberli, F., Audétat, A., Guillong, M., Simon, A.C., Hanley, J.J., Klemm, L.M., 2012. Recent developments in element concentration and isotope ratio analysis of individual fluid inclusions by laser ablation single and multiple collector ICP-MS. Ore Geol. Rev. https://doi.org/10.1016/j.oregeorev.2011.11.001.

Pozebon, D., Scheffler, G.L., Dressler, V.L., 2017. Recent applications of laser ablation inductively coupled plasma mass spectrometry (LA-ICP-MS) for biological sample analysis: A follow-up review. J. Anal. At. Spectrom. https://doi.org/10.1039/c7ja00026j.

Pyle, J.M., Spear, F.S., 2003. Four generations of accessory-phase growth in low-pressure migmatites from SW New Hampshire. Am. Mineral. 88, 338–351. https://doi.org/10.2138/am-2003-2-311.

Raimondo, T., Payne, J., Wade, B., Lanari, P., Clark, C., Hand, M., 2017. Trace element mapping by LA-ICP-MS: assessing geochemical mobility in garnet. Contrib. to Mineral. Petrol. 172. https://doi.org/10.1007/s00410-017-1339-z.

Rasbury, E.T., Cole, J.M., 2009. Directly dating geologic events: U-Pb dating of carbo-nates. Rev. Geophys. https://doi.org/10.1029/2007RG000246.

Ritchie, N.W.M., Newbury, D.E., Davis, J.M., 2012. EDS measurements of X-ray intensity at WDS precision and accuracy using a silicon drift detector. In: Microscopy and Microanalysis. pp. 892–904. https://doi.org/10.1017/S1431927612001109.

Rittner, M., Müller, W., 2012. 2D mapping of LA-ICPMS trace element distributions using R. Comput. Geosci. 42, 152–161. https://doi.org/10.1016/j.cageo.2011.07.016.

Rivers, T., 2012. Upper-crustal orogenic lid and mid-crustal core complexes: Signature of a collapsed orogenic plateau in the hinterland of the Grenville Province. Can. J. Earth Sci. 49, 1–42. https://doi.org/10.1139/E11-014.

Roberts, N.M.W., Walker, R.J., 2016. U-Pb geochronology of calcite-mineralized faults: Absolute timing of rift-related fault events on the northeast Atlantic margin. Geology 44, 531–534. https://doi.org/10.1130/G37868.1.

Roberts, N.M.W., Drost, K., Horstwood, M.S.A., Condon, D.J., Chew, D., Drake, H., Milodowski, A.E., McLean, N.M., Smye, A.J., Walker, R.J., Haslam, R., Hodson, K., Imber, J., Beaudoin, N., Lee, J.K., 2020. Laser ablation inductively coupled plasma mass spectrometry (LA-ICP-MS) U-Pb carbonate geochronology: strategies, progress, and limitations. Geochronology 2, 33–61. https://doi.org/10.5194/gchron-2-33-2020.

Ronzani, A.L., Pointurier, F., Rittner, M., Borovinskaya, O., Tanner, M., Hubert, A., Humbert, A.C., Aupiais, J., Dacheux, N., 2018. Capabilities of laser ablation-ICP-TOF-MS coupling for isotopic analysis of individual uranium micrometric particles. J. Anal. At. Spectrom. 33, 1892–1902. https://doi.org/10.1039/c8ja00241j.

Rusk, B., Koenig, A., Lowers, H., 2011. Visualizing trace element distribution in quartz using cathodoluminescence, electron microprobe, and laser ablation-inductively coupled plasma-mass spectrometry. Am. Mineral. 96, 703–708. https://doi.org/10.2138/am.2011.3701.

Šala, M., Šelih, V.S., Stremtan, C.C., van Elteren, J.T., 2020. Analytical performance of a

high-repetition rate laser head (500 Hz) for HR LA-ICP-QMS imaging. J. Anal. At. Spectrom. https://doi.org/10.1039/c9ja00421a.

Spear, F.S., Pyle, J.M., 2010. Theoretical modeling of monazite growth in a low-Ca metapelite. Chem. Geol. 273, 111–119. https://doi.org/10.1016/j.chemgeo.2010.02.016.

Spencer, K.J., Hacker, B.R., Kylander-Clark, A.R.C., Andersen, T.B., Cottle, J.M., Stearns, M.A., Poletti, J.E., Seward, G.G.E., 2013. Campaign-style titanite U-Pb dating by laser-ablation ICP: Implications for crustal flow, phase transformations and titanite closure. Chem. Geol. 341, 84–101. https://doi.org/10.1016/j.chemgeo.2012.11.012.

Stead, C.V., Tomlinson, E.L., McKenna, C.A., Kamber, B.S., 2017. Rare earth element partitioning and subsolidus exchange behaviour in olivine. Chem. Geol. 475, 1–13. https://doi.org/10.1016/j.chemgeo.2017.10.020.

Steadman, J.A., Large, R.R., Meffre, S., Olin, P.H., Danyushevsky, L.V., Gregory, D.D., Belousov, I., Lounejeva, E., Ireland, T.R., Holden, P., 2015. Synsedimentary to early diagenetic gold in Black shale-hosted pyrite nodules at the Golden Mile deposit, Kalgoorlie, Western Australia. Econ. Geol. 110, 1157–1191. https://doi.org/10.2113/econgeo.110.5.1157.

Stern, R., 2009. An introduction to secondary ion mass spectrometry (SIMS) In: Geology. Secondary Ion Mass Spectrometry in the Earth Sciences: Gleaning the big picture from a small spot. Mineral Assoc. Can Short Course 41, 1–18.

Su, S.Q., Qin, K.Z., Li, G.M., Olin, P., Thompson, J., 2019. Cathodoluminescence and trace elements of scheelite: Constraints on ore-forming processes of the Dabaoshan porphyry Mo-W deposit. South China. Ore Geol. Rev. 115. https://doi.org/10.1016/j.oregeorev.2019.103183.

Suhr, N., Schoenberg, R., Chew, D., Rosca, C., Widdowson, M., Kamber, B.S., 2018. Elemental and isotopic behaviour of Zn in Deccan basalt weathering profiles: Chemical weathering from bedrock to laterite and links to Zn deficiency in tropical soils. Sci. Total Environ. 619–620, 1451–1463. https://doi.org/10.1016/j.scitotenv.2017.11.112.

Suzuki, T., Sakata, S., Makino, Y., Obayashi, H., Ohara, S., Hattori, K., Hirata, T., 2018. iQuant2: Software for Rapid and Quantitative Imaging Using Laser Ablation-ICP Mass Spectrometry. Mass Spectrom. 7, A0065. https://doi.org/10.5702/massspectrometry.a0065.

Sylvester, P.J., Jackson, S.E., 2016. A brief history of laser ablation inductively coupled plasma mass spectrometry (LA-ICP-MS). Elements 12, 307–310. https://doi.org/10.2113/gselements.12.5.307.

Teledyne CETAC Technologies, 2020. HDIP LA-ICP-MS Image Processing Software [WWW Document]. URL. http://www.teledynecetac.com/products/laser-ablation/hdip-imaging-software (accessed 11.7.19).

Timms, N.E., Kirkland, C.L., Cavosie, A.J., Rae, A.S.P., Rickard, W.D.A., Evans, N.J., Erickson, T.M., Wittmann, A., Ferrière, L., Collins, G.S., Gulick, S.P.S., 2020. Shocked titanite records Chicxulub hydrothermal alteration and impact age. Geochim. Cosmochim. Acta 281, 12–30. https://doi.org/10.1016/j.gca.2020.04.031.

Treble, P.C., Chappell, J., Shelley, J.M.G., 2005. Complex speleothem growth processes revealed by trace element mapping and scanning electron microscopy of annual layers. Geochim. Cosmochim. Acta 69, 4855–4863. https://doi.org/10.1016/j.gca.2005.06.008.

Ubide, T., Kamber, B.S., 2018. Volcanic crystals as time capsules of eruption history. Nat. Commun. 9. https://doi.org/10.1038/s41467-017-02274-w.

Ubide, T., McKenna, C.A., Chew, D.M., Kamber, B.S., 2015. High-resolution LA-ICP-MS trace element mapping of igneous minerals: In search of magma histories. Chem. Geol. 409, 157–168. https://doi.org/10.1016/j.chemgeo.2015.05.020.

Ubide, T., Mollo, S., Zhao, J. Xin, Nazzari, M., Scarlato, P., 2019a. Sector-zoned clinopyroxene as a recorder of magma history, eruption triggers, and ascent rates. Geochim. Cosmochim. Acta 251, 265–283. https://doi.org/10.1016/j.gca.2019.02.021.

Ubide, T., Caulfield, J., Brandt, C., Bussweiler, Y., Mollo, S., Di Stefano, F., Nazzari, M., Scarlato, P., 2019b. Deep Magma Storage Revealed by Multi-Method Elemental Mapping of Clinopyroxene Megacrysts at Stromboli Volcano. Front. Earth Sci. 7. https://doi.org/10.3389/feart.2019.00239.

Ulrich, T., Kamber, B.S., Jugo, P.J., Tinkham, D.K., 2009. Imaging element-distribution patterns in minerals by laser ablation - Inductively coupled plasma - Mass spectrometry (LA-ICP-MS). Can. Mineral. 47, 1001–1012. https://doi.org/10.3749/canmin.47.5.1001.

Urgast, D.S., Ou, O., Gordon, M.J., Raab, A., Nixon, G.F., Kwun, I.S., Beattie, J.H., Feldmann, J., 2012. Microanalytical isotope ratio measurements and elemental mapping using laser ablation ICP-MS for tissue thin sections: Zinc tracer studies in rats. MAnal. Bioanal. Chem. 402, 287–297. https://doi.org/10.1007/s00216-011-5461-x.

Van Breemen, O., Davidson, A., Overidge, W.D., Sullivan, R.W., 1986. U-Pb zircon geochronology of Grenville tectonites, granulites and igneous precursors, Parry Sound, Ontario. In: Moore, J.M., Davidson, A., Baer, A.J. (Eds.), The Grenville Province. Geological Association Canada Special Paper. 31. pp. 191–207.

Van Elteren, J.T., Izmer, A., Šelih, V.S., Vanhaecke, F., 2016. Novel Image Metrics for Retrieval of the Lateral Resolution in Line Scan-Based 2D LA-ICPMS Imaging via an Experimental-Modeling Approach. Anal. Chem. 88, 7413–7420. https://doi.org/10.1021/acs.analchem.6b02052.

Van Elteren, J.T., Šelih, V.S., Šala, M., Van Malderen, S.J.M., Vanhaecke, F., 2018. Imaging Artifacts in Continuous Scanning 2D LA-ICPMS Imaging Due to Nonsynchronization Issues. Anal. Chem. 90, 2896–2901. https://doi.org/10.1021/acs.analchem.7b05134.

Van Elteren, J.T., Šelih, V.S., Šala, M., 2019. Insights into the selection of 2D LA-ICP-MS (multi)elemental mapping conditions. J. Anal. At. Spectrom. 34, 1919–1931. https://doi.org/10.1039/c9ja00166b.

Van Malderen, S.J.M., Van Elteren, J.T., Vanhaecke, F., 2015. Development of a fast laser ablation-inductively coupled plasma-mass spectrometry cell for sub-µm scanning of layered materials. J. Anal. At. Spectrom. 30, 119–125. https://doi.org/10.1039/c4ja00137k.

Van Malderen, S.J.M., Managh, A.J., Sharp, B.L., Vanhaecke, F., 2016. Recent developments in the design of rapid response cells for laser ablation-inductively coupled plasma-mass spectrometry and their impact on bioimaging applications. J. Anal. At. Spectrom. 31, 423–439. https://doi.org/10.1039/C5JA00430F.

Van Malderen, S.J.M., Laforce, B., Van Acker, T., Nys, C., De Rijcke, M., De Rycke, R., De Bruyne, M., Boone, M.N., De Schamphelaere, K., Borovinskaya, O., De Samber, B., Vincze, L., Vanhaecke, F., 2017a. Three-Dimensional Reconstruction of the Tissue-Specific Multielemental Distribution within Ceriodaphnia dubia via Multimodal Registration Using Laser Ablation ICP-Mass Spectrometry and X-ray Spectroscopic Techniques. Anal. Chem. 89, 4161–4168. https://doi.org/10.1021/acs.analchem.7b00111.

Van Malderen, S.J.M., Laforce, B., Van Acker, T., Vincze, L., Vanhaecke, F., 2017b. Imaging the 3D trace metal and metalloid distribution in mature wheat and rye grains: Via laser ablation-ICP-mass spectrometry and micro-X-ray fluorescence spectrometry. J. Anal. At. Spectrom. 32, 289–298. https://doi.org/10.1039/c6ja00357e.

Van Malderen, S.J.M., van Elteren, J.T., Šelih, V.S., Vanhaecke, F., 2018. Considerations on data acquisition in laser ablation-inductively coupled plasma-mass spectrometry with low-dispersion interfaces. Spectrochim. Acta - Part B At. Spectrosc. 140, 29–34. https://doi.org/10.1016/j.sab.2017.11.007.

Van Malderen, S.J.M., Van Acker, T., Vanhaecke, F., 2020. Sub-micrometer Nanosecond LA-ICP-MS Imaging at Pixel Acquisition Rates above 250 Hz via a Low-Dispersion Setup. Anal. Chem. 92, 5756–5764. https://doi.org/10.1021/acs.analchem.9b05056.

Webb, G.E., Kamber, B.S., 2011. Trace element geochemistry as a tool for interpreting microbialites, in: Earliest Life on Earth: Habitats, Environments and Methods of Detection. pp. 127–170. https://doi.org/10.1007/978-90-481-8794-2_6.

Weiskirchen, R., Weiskirchen, S., Kim, P., Winkler, R., 2019. Software solutions for evaluation and visualization of laser ablation inductively coupled plasma mass spectrometry imaging (LA-ICP-MSI) data: A short overview. J. Cheminform. https://doi.org/10.1186/s13321-019-0338-7.

Wilkinson, J.J., Chang, Z., Cooke, D.R., Baker, M.J., Wilkinson, C.C., Inglis, S., Chen, H., Bruce Gemmell, J., 2015. The chlorite proximitor: A new tool for detecting porphyry ore deposits. J. Geochemical Explor. 152, 10–26. https://doi.org/10.1016/j.gexplo.2015.01.005.

Williams, M.L., Jercinovic, M.J., Hetherington, C.J., 2007. Microprobe Monazite Geochronology: Understanding Geologic Processes by Integrating Composition and Chronology. Annu. Rev. Earth Planet. Sci. 35, 137–175. https://doi.org/10.1146/annurev.earth.35.031306.140228.

Williams, M.L., Jercinovic, M.J., Mahan, K.H., Dumond, G., 2017. Electron Microprobe Petrochronology, in: Kohn, M.J., Engi, M., Lanari, P. (Eds.), Petrochronology: Methods and Applications. Reviews in Mineralogy and Geochemistry 83 (1), 153–182. https://doi.org/10.2138/rmg.2017.83.5.

Woodhead, J., Petrus, J., 2019. Exploring the advantages and limitations of in situ U-Pb carbonate geochronology using speleothems. Geochronology 1, 69–84. https://doi.org/10.5194/gchron-1-69-2019.

Woodhead, J.D., Hellstrom, J., Hergt, J.M., Greig, A., Maas, R., 2007. Isotopic and elemental imaging of geological materials by laser ablation inductively coupled plasma-mass spectrometry. Geostand. Geoanalytical Res. 31, 331–343. https://doi.org/10.1111/j.1751-908X.2007.00104.x.

Woodhead, J.D., Horstwood, M.S.A., Cottle, J.M., 2016. Advances in isotope ratio determination by LA-ICP-MS. Elements 12, 317–322. https://doi.org/10.2113/gselements.12.5.317.

Wu, Y.F., Li, J.W., Evans, K., Koenig, A.E., Li, Z.K., O'Brien, H., Lahaye, Y., Rempel, K., Hu, S.Y., Zhang, Z.P., Yu, J.P., 2018. Ore-forming processes of the Daqiao epizonal orogenic gold deposit, West Qinling Orogen, China: Constraints from textures, trace elements, and sulfur isotopes of pyrite and marcasite, and raman spectroscopy of carbonaceous material. Econ. Geol. 113, 1093–1132. https://doi.org/10.5382/econgeo.2018.4583.

Yakymchuk, C., Clark, C., White, R.W., 2017. Phase Relations, Reaction Sequences and Petrochronology, in: Kohn, M.J., Engi, M., Lanari, P. (Eds.), Petrochronology: Methods and Applications. Reviews in Mineralogy and Geochemistry 83 (1), 13–53. https://doi.org/10.2138/rmg.2017.83.2.

Yao, M., Cao, Y., Liu, J., Ren, Z., 2017. Magma mixing as a trigger for sulphide saturation in the UG2 chromitite (bushveld): Evidence from the silicate and sulphide melt inclusions in chromite. Acta Geologica Sinica - English Edition 91, 1704–1716. https://doi.org/10.1111/1755-6724.13406.

Zhao, J., Liang, J., Li, Jie, Huang, Y., Liu, X., Zhang, J., Hao, J., Sun, W., Li, Jianzhong, Xie, J., 2020. Gold and sulfur sources of the Taipingdong Carlin-type gold deposit: Constraints from simultaneous determination of sulfur isotopes and trace elements in pyrite using nanoscale secondary ion mass spectroscopy. Ore Geol. Rev. 117. https://doi.org/10.1016/j.oregeorev.2019.103299.

Zhou, L., McKenna, C.A., Long, D.G.F., Kamber, B.S., 2017. LA-ICP-MS elemental mapping of pyrite: An application to the Palaeoproterozoic atmosphere. Precambrian Res. 297, 33–55. https://doi.org/10.1016/j.precamres.2017.05.008.

Zhu, Z.Y., Cook, N.J., Yang, T., Ciobanu, C.L., Zhao, K.D., Jiang, S.Y., 2016. Mapping of sulfur isotopes and trace elements in sulfides by LA-(MC)-ICP-MS: Potential analytical problems, improvements and implications. Minerals 6. https://doi.org/10.3390/min6040110.